Additive Manufacturing 46 (2021) 102143

Contents lists available at ScienceDirect

Additive Manufacturing

journal homepage: www.elsevier.com/locate/addma

Research Paper

Designing additively manufactured lattice structures based on deformation mechanisms

Behzad Bahrami Babamiri [a], Baxter Barnes [a], Arash Soltani-Tehrani [b,d], Nima Shamsaei [b,d], Kavan Hazeli [a,c,*]

[a] Mechanical and Aerospace Engineering Department, University of Alabama in Huntsville, USA
[b] Department of Mechanical Engineering, Auburn University, USA
[c] Aerospace and Mechanical Engineering Department, The University of Arizona, USA
[d] National Center for Additive Manufacturing Excellence (NCAME), Auburn University, USA

ARTICLE INFO

Keywords:
Lattice structure
Additive manufacturing
Deformation mechanisms
Volumetric hardening model
Optimization
Microstructure

ABSTRACT

The post-yield mechanical behavior of additively manufactured lattice structures (AMLS) is governed by the interplay between intrinsic (microstructural) and extrinsic (structural topology) properties at different length scales. Herein, we introduce a novel design optimization approach that accounts for scale separation and size effects, which control deformation mechanisms, to achieve a certain targeted macroscopic mechanical response. The new topological designs are guided by finding a direct correlation between the distribution of local stresses within struts and the underlying microstructures. The local stresses are computed using a strut-level yield criterion that has been calibrated to strut-level tensile, compressive, and shear loading experiments. Therefore, the local response of the struts, including tension-compression asymmetry, build direction dependence, and size effects, are accounted for in the yield surface, enabling a more accurate representation of the local stress state. Accurate calculation of the stress state for a given microstructure and topology combination allows for optimizing the topology for the given strut-level microstructure. The interplay between the topology and microstructure is assessed by investigating the unit cell-level deformation mechanisms and quantifying their influence on the global stress-strain relationship via finite element simulations. Using these relationships, a new set of topologies is designed, built, and validated with experiments. On average, the new topologies demonstrate 40% and 72% improvement in energy absorption capacity and flow stress, respectively, compared to topologies that had been previously optimized using constitutive models, which are homogeneous throughout the unit cell. The goal of the presented article is to demonstrate that simultaneously considering the effects of topology and microstructure on the mechanical behavior of AMLS has the potential to substantially improve key performance metrics, including ultimate strength and energy dissipation. The distinguishing and novel feature of our approach is that the topological optimization is performed while accounting for the heterogeneous distribution of strut-level microstructural features and concomitant mechanical behavior, which leads to new insights relative to peak AMLS structural performance.

1. Introduction

Multi-functionality and lightweight are two fundamental characteristics of additively manufactured (AM) lattice structures (LS), or AMLS, that can be achieved by design and optimization methods. Lattice structures are three-dimensional (3D) structures formed by repeating unit cells, which consist of a network of struts connected at nodes (see Fig. 1). The periodic nature of the constituent unit cell differentiates LS from other classes of cellular materials such as metallic foams. Therefore, unit cell configuration, which depends on strut dimensions and orientation angles, can be used as a design variable for mechanical property optimization. In general, property optimization of materials with hierarchical structures can be divided into three main categories: (1) optimization of unit cell shape, (2) optimization of the unit cell size distribution, (3) optimization of unit cell parameters (such as strut dimensions). The differences between each of these optimization

* Corresponding author at: Aerospace and Mechanical Engineering Department, The University of Arizona, USA.
E-mail address: hazeli@arizona.edu (K. Hazeli).

https://doi.org/10.1016/j.addma.2021.102143
Received 7 January 2021; Received in revised form 19 June 2021; Accepted 22 June 2021
Available online 28 June 2021

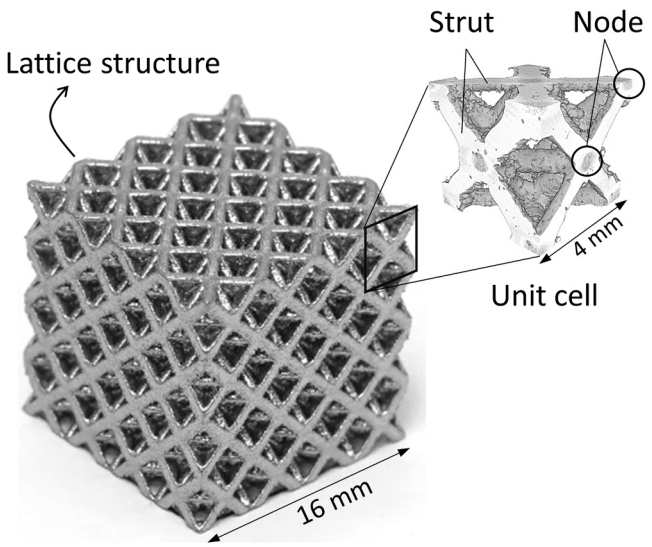

Fig. 1. AMLS with Octet truss topology formed by a repeated arrangement of spatial unit cells composed of struts and nodes.

categories mainly depend on the definition of the design variables, which are the parameters that can be changed during the optimization process [1,2]. Furthermore, for each category, there are several different optimization approaches. For instance, in the unit cell optimization method, the unit cell shape, structure, and spatial arrangement (periodic, stochastic, or hierarchical tessellation) are the design variables for structures ranging from prismatic hexagonal honeycomb and stochastic foams to LS. In other words, different unit cell structures with different shapes are designed using CAD software; subsequently, the performance and behavior of those unit cells are examined by analytical (Maxwell's stability criterion [3] or Gibson-Ashby [4]), empirical (experimental), or computational methods (finite element simulation) [5–8,9]. Once the desired performance is achieved, the aggregate LS is fabricated using the arrangement of unit cells best determined to meet project requirements.

Optimization of unit cell size, topology, and distribution has also been inspired by nature. Material gradients commonly occur in cellular biological materials such as bone, sea sponges, teeth, bamboo, pine leaves, and horses hooves [10]. In nature multi-functionality is achieved by adapting to the local loading conditions and relying on building hierarchical structures with the optimized spatial distribution of unit cells with varying sizes as needed to maximize accommodation of local stresses. Mimicking natural structures by selecting the best spatial variation of cell sizes for a specific loading condition is another design challenge that can be guided by examining the local response of different unit cells with selected relative densities throughout a design [4]. Regular and functionally graded periodic structures (i.e. error diffusion method [11]) and stochastic structures implementing sizing distribution rules (such as the top-down Voronoi-tessellation method [12]) are examples of proposed unit cell size distribution strategies to create graded cellular material. The Voronoi-tessellation method is an innovative way to control the unit cell size, density, local distribution, and morphology without producing material discontinuities [12–14]. Therefore, it can be implemented to generate LS with regular or functionally graded distributions of porosity and unit cell size [15]. This approach is one of the most effective ways to mimic the cellular structures in natural tissues such as bone [16]. Another benefit of implementing graded materials into LS is that graded cellular materials can achieve greater energy absorption capacity than regular cellular structures [17].

The optimization of unit cell parameters, including struts dimensions, topology, and microstructure are design variables of concern for the present investigation. For example, in LS, unit cell parameters include strut length, thickness, cross-sectional shape and area, fillet radius at the nodes, and the building material properties. The relative density-based scaling law relationship introduced by Ashby et al. [4,18] is one of the most widely used methods to determine the optimized thickness parameter of simple cellular material geometries. There are some drawbacks in the relative density approach, however, as it overlooks critical geometrical factors such as strut geometry [19–22] and fillet radii at the nodes [23,24].

Tang and Zhao [25] used a genetic algorithm to optimize the distribution of struts orientation angles inside a lattice structure. In this method, the overall volume of the structure is divided into several subsections. An equivalent analysis model is created by considering the effective orthotropic properties of LS at the macroscopic level. Then, a genetic algorithm is applied to measure the optimized distribution of minimum strain energy and higher structural stiffness by regulating the struts orientation angles. The results from [25], indicates that an optimized LS designed with non-uniform strut orientation angles was more stiffness efficient (i.e., had higher stiffness per unit mass) than LS with uniform strut orientation angles. Homogenization-based topology optimization combined with field-aligned parameterization [26] is another method to optimize LS topology using the distribution of struts orientation to enhance stiffness. This method optimizes the structural stiffness of LS by aligning the struts with principal stress directions. In this approach, the struts on the boundary match the curved surfaces of the optimized 3D shapes. This method resulted in an LS with a critical buckling load approximately twice that of a topology-optimized solid structure at the cost of a slight decrease in stiffness.

Wu et al. [27] used the Approximation of Reduced Substructure with Penalization (ARSP) model to improve LS manufacturability and stiffness by solving connectivity and length scale-ratio problems that arise in conventional homogenization-based methods. In the ARSP method, the structure is assumed to be made of multiple substructures that consist of the same unit cell topology in two different, connected length scales. As substructure density is a design variable in this process, the geometry of the LS in each substructure can be changed by changing the associated density. This process offers the potential to produce stiffness-efficient LS with improved manufacturability. Feng et al. [28] employed a two-stage topology optimization strategy for LS. This process optimizes strut mass by altering the nodal x- and y-coordinates and grid configuration. A genetic algorithm is used to adjust nodal coordinates and remove struts under low stress from the structure. This technique results in a weight-efficient LS at the expense of stiffness and nonlinear buckling load.

Chen et al. [29] employed an FE method-based technique to generate large-scale, weight-optimized LS. The LS nodes for a given geometry are defined horizontally, and the desired unit cell is created by connecting these nodes with struts. The initial lattice structure is assembled by connecting a specified number of unit cells in each direction. The mesh configuration method is used to remove struts under low stress from the structure, resulting in an optimized structure demonstrating superior stiffness over the initial structure. Global stiffness was shown to improve by 11.83% by implementing this process, although further investigation is required to evaluate the proposed method's efficiency and effectiveness over existing techniques. Du et al. [30] used an energy-based homogenization method to find the optimal distribution of material phases within the unit cell of the periodic LS. This topology optimization strategy aims to improve the transverse shear performance of the hexagonal unit cells. Their results show improvement in the shear stiffness and bearing properties of the optimized LS compared to the traditional honeycomb sandwich structure.

2. Significance and need for developing a new optimization technique

While optimization methods developed for hierarchical materials, such as those summarized in Section 1 and others [31–34–37], have also

improved weight-efficiency and stiffness in AMLS, these optimization methods do not account for characteristic material behaviors such as plastic anisotropy resulting from the microstructure of AMLS constituents. It is important to note that the focus of the many studies mentioned above is placed only on the elastic regime of the hierarchical materials, so parameters which control yielding and subsequent plastic stress flow are mainly unexplored. Therefore, in this study we show that by considering the combined effects of microstructure and topology on the mechanical properties of additively manufactured lattice structures, novel designs may be discovered through the presented optimization methods that otherwise would be overlooked if topology alone is considered. As a demonstration of our design strategy, we will establish the connection between microstructure and mechanical behavior through experiments and show how using microstructure-specific material properties in unit cell analysis influences the development of local stresses, plasticity, and damage evolution as a function of topology. Once the interplay between topology and microstructure on the mechanical behavior of AMLS is understood, we limit the adverse effects of each attribute by designing a new lattice topology that leads to enhanced yield strength and energy absorption capacity relative to topologies optimized using constitutive models, which are homogeneous throughout the unit cell. Specifically, our analysis shows that optimization of topological features including struts angle and thickness can be guided by microstructural effects, such as increased yield strength, while avoiding the limitations imposed by the microstructure on the mechanical behavior, e.g., low ductility.

Altering the microstructure through heat treatments may be used to improve the mechanical behavior of AMLS [38]. However, this may lead to unexpected behavior such as a drop in plastic flow stress at some stages of deformation. For instance, Fig. 2 compares the quasi-static compression behavior of AM IN718 Octet truss (OT) and Rhombic dodecahedron (RD) lattice structures with 30% relative density with either as-built (AB) or solution treated and aged (STA) microstructures. Fig. 2 shows that changing the strut microstructure through heat treatment improved the yield strength by approximately 38% and 46% in OT and RD, respectively (see Fig. 2c & d). While the yield strength was improved, the STAs microstructure led to a drastic drop in the plastic flow stress in both topologies: ≈ 50% drop in OT specimens and ≈ 17% drop in RD specimens. The design strategy proposed in this article aims to improve the mechanical response of AMLS, including flow stress and energy absorption capacity, by using benefits of microstructural control (through heat treatment) to enhance the yield strength while using topology to overcome microstructural shortcomings in flow stress retention, resulting in a high yield strength coupled with maintained high flow stress, ultimately leading to improved energy absorption capacity.

3. Material systems and experimental procedure

3.1. Manufacturing and heat-treatment

In the present study, argon atomized Inconel 718 (IN718) powder was used to fabricate parts. The chemical composition, adapted from [39], is reported in Table 1. All parts were manufactured using an EOS M290 machine, which is equipped with a Ytterbium (Yb) fiber laser. All parts were manufactured under an inert argon atmosphere using EOS recommended process parameters (see Table 2).

As seen in Fig. 3, three layouts were used to fabricate LS as well as the bulk structures. In the first set of specimens, 72 LS with three different topologies were manufactured (see Fig. 3a). All parts were slightly oriented on the build plate to minimize the disturbance caused by the recoater during fabrication. In the second set of specimens, four vertical tension, compression, and shear specimens were fabricated, along with four diagonal tension specimens (see Fig. 3b). Finally, several tension and compression specimens with different thicknesses in both vertical and diagonal directions and four vertical shear specimens were fabricated in the third set of specimens (see Fig. 3c).

After fabrication, all parts were detached from the build plates. Some parts were tested in the AB condition without any further post-

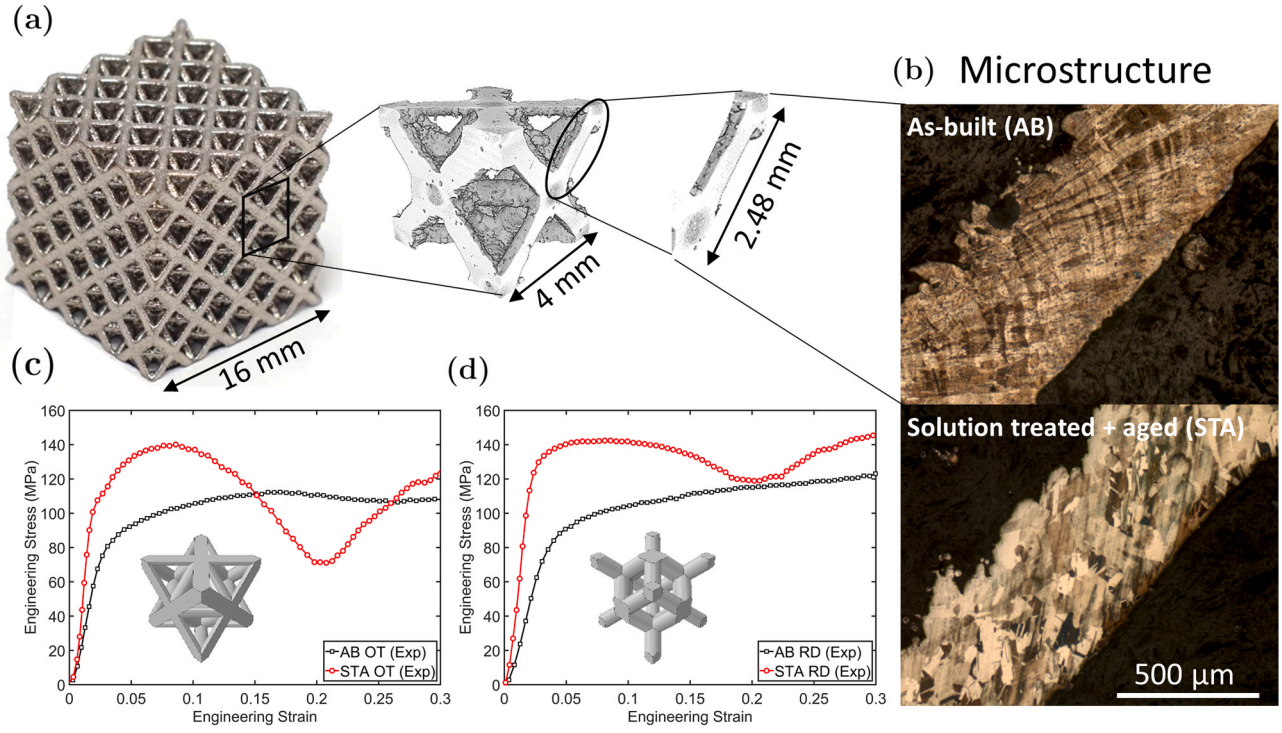

Fig. 2. The effect of solution treatment and aging on the quasi-static compression behavior of AMLS with OT and RD topology made of IN718. (a) the schematic of AMLS with unit cell and strut dimensions, (b) the struts' microstructure including grain size and morphology for AB and STA specimens are compared and correlated to the mechanical properties of (c) OT ($\rho^* = 30\%$) and (d) RD ($\rho^* = 30\%$) topologies under quasi-static compression loading. Both OT and RD specimens experienced a peak compressive stress at around 5% strain, followed by a sharp drop in flow stress for the STA specimens.

Table 1
Chemical composition of IN718 based on ASTM F3055 [39].

Element	ASTM F3055
Carbon (C)	0.08 (Max)
Manganese (Mn)	0.35 (Max)
Silicon (Si)	0.35 (Max)
Phosphorus (P)	0.015 (Max)
Sulfur (S)	0.015 (Max)
Chromium (Cr)	17.00–21.00
Cobalt (Co)	1.00 (Max)
Molybdenum (Mo)	2.80–3.30
Niobium + tantalum (Nb+Ta)	4.75–5.50
Titanium (Ti)	0.65–1.15
Aluminum (Al)	0.20–0.80
Iron (Fe)	Remainder
Copper (Cu)	0.30 (Max)
Nickel (Ni)	50.00–55.00
Boron (B)	0.006 (Max)

Table 2
Material, laser parameters, and scan strategy used in the manufacture of AM IN718.

Material	Inconel 718
Core laser power (W)	285
Core scan speed (mm/s)	960
Outside counter laser power (W)	80
Outside counter scan speed (mm/s)	800
Inside counter laser power (W)	138
Inside counter scan speed (mm/s)	300
Stripe distance (Hatch distance) (mm)	0.11
Stripe width (mm)	10
Build layer thickness (mm)	0.04
Layer rotation angle	67°
Energy density (J/mm^3)	67.47
Beam comp (mm)	0.015

processing heat treatments. The rest of the specimens underwent a stress-relieving heat treatment according to ASTM F3055 at 1065 °C for 1.5 h [39] followed by furnace cooling. Afterward, some parts were removed from the batch to be tested in the stress relieved (SR) condition. Finally, the remainder of the structures were subjected to the STA heat treatment. STA parts were homogenized at 1065 °C for 1.5 h followed by argon purge cooling. The STA specimens were then aged at 760 °C for 10 h, followed by furnace cooling to 650 °C. Finally, STA specimens were held at this temperature for a total precipitation time of 20 h and cooled by argon purging.

3.2. Quasi-static mechanical testing

Quasi-static tension and compression testing were performed using a servo-hydraulic Materials Testing System (MTS) machine with a 100 kN load cell. The displacement rate was set to 1 mm per minute for both tension and compression tests, corresponding to strain rates on the order of $10^{-4}\ s^{-1}$ to $10^{-3}\ s^{-1}$. Tensile tests were run until the samples fractured; compression tests were run until the desired deformation was reached, approximately 5 mm in the bulk compression samples and 10 mm in the AMLS compression samples. In addition, quasi-static shear testing was performed using a Satec Model 120HVL under NASM 1312–13. The load was applied at a rate of 68.5 kN/min with a span of 12.5 mm. At least two tests were run for each specimen type and heat treatment to ensure repeatability of the results.

Digital image correlation (DIC) techniques were used to calculate strain using Correlated Solution's Vic 2D software. A PointGrey Grasshopper camera (model number GS3-U3–51S5M-C) with a resolution of 2448 × 2048 pixels was used to perform the imaging. Samples were lightly polished, and a DIC speckle pattern was applied using an airbrush. The specimens were sprayed with a layer of white paint followed by a misting with black paint to produce a random speckle pattern. Images were taken at a frame rate of 20 frames per second during the elastic deformation stage, with subsequent images taken at a frame rate of 1 frame per second until the conclusion of the test. A Cole-Parmer 41500–50 fiber optic illuminator was used to illuminate the samples. For DIC analysis, a subset size of 33 pixels and a step size of 11 pixels were used. A series of images taken before sample loading was used to calculate the uncertainty of the DIC strain measurements. The standard deviation of the unloaded strain was calculated to be 245 $\mu\epsilon$ for the tensile samples and 635 $\mu\epsilon$ for the compression samples.

4. Introducing a new optimized topology based on deformation mechanisms

This section delineates the basis of an optimization approach that accounts for the combined effects of microstructure and topology. The optimization process introduced here attempts to improve the mechanical strength of topologies previously optimized using classical optimization theories for the unit cells. Historically, geometric considerations and beam element mechanics have been used to find an optimized balance between strength, stiffness, and weight in OT and RD topologies. In the following sections, the process of designing new topologies guided by deformation mechanisms is explained. To provide a consistent comparison with previous topologies, the relative density is held constant at 30% in the newly developed topologies, still exhibiting considerable improvements in yield strength, strain hardening rate and energy absorption capacity. The design strategy relies on understanding and subsequently controlling the local unit cell-level deformation mechanisms. The effects of the magnitude and distribution of the local stresses rising from local response of the microstructure (e.g., plastic anisotropy) on the global response are calculated at different stages of deformation, and a relationship between local instability and macroscopic behavior is established. To obtain accurate values of local stresses, it is first necessary to define a proper material model. In this study, the material model is represented with a yield surface whose evolution, i.e., hardening and softening, is governed by the modified volumetric hardening model (VHM), or MVHM [40], which was

Fig. 3. (a) The lattice structure samples before heat-treatment, (b) the quasi-static tension, compression, and shear samples and their build direction, (c) the quasi-static tension, compression, and shear samples with different build direction and thicknesses.

originally introduced by Deshpande and Fleck [41]. The main advantage of MVHM over VHM in the case of AMLS is that the yield surface is assigned to the respective struts, thus enabling capture of the hardening and softening of the flow stress curves as deformation proceeds while accounting for (1) tension-compression asymmetry of strut-level response; (2) tension-compression asymmetry of the aggregate response; and (3) hydrostatic pressure sensitivity of the strut-level response [40].

4.1. Experimentally driven customized yield surface for AMLS

The yield surface for MVHM is described in terms of von Mises stress σ_v, and hydrostatic pressure (p), i.e. $F(p, \sigma_v)$:

$$F(p,\sigma_v) = \sqrt{\sigma_v^2 + \alpha^2 (p - p_0)^2} - B = 0 \tag{1}$$

The yield surface expressed in Eq. (1) evolves in a self-similar manner (i.e. α is constant). p_0 is the center of the yield ellipse on the p-axis and B is the size of the (vertical) σ_v-axis of the yield ellipse. α, p_0, and B are defined as follows:

$$\alpha = \frac{3\sigma_c}{\sqrt{(3p_t + \sigma_c)(3p_c - \sigma_c)}}$$

$$p_0 = p_c - p_t/2$$

$$B = \alpha(p_c + p_t/2).$$

The von Mises stress (σ_v) and the pressure stress (p) in the Eq. (1) are defined is Eq. (2) and (3), respectively.

$$\sigma_v = \sqrt{\frac{3}{2}\sigma_{dev} : \sigma_{dev}} \tag{2}$$

$$p = -\frac{1}{3}\, trace\ \sigma \tag{3}$$

Where σ_c is compressive yield strength, and p_c and p_t are yield strength in hydrostatic compression and yield strength in hydrostatic tension, respectively.

Substituting α, p_0, B into Eq. (1) gives:

$$F(p,\sigma_v) = \sqrt{\sigma_v^2 + \frac{9\sigma_c^2}{(3p_t + \sigma_c)(3p_c - \sigma_c)}\left(p - \left(\frac{p_c - p_t}{2}\right)\right)^2} - \frac{3\sigma_c}{\sqrt{(3p_t + \sigma_c)(3p_c - \sigma_c)}}\left(\frac{p_c + p_t}{2}\right) = 0 \tag{4}$$

The values of p_c, p_t, and σ_c are in Eq. (4) are unknown. Therefore, to create the yield surface, at least three distinct points or three different loading paths are required [40]. In this study, yield strengths in tension, compression, and shear are chosen as three different points to generate the initial yield surface (see Fig. 4). These quantities are used because quasi-static tension, compression, and shear testing setups are usually more readily available than combined hydrostatic compression and tension tests. It should be noted that fitting to the yield functions is possible only if the number of loading directions is equal to or larger than the number of parameters of the yield functions (i.e., 3). The required fitting procedure to establish the initial yield surface using the yield point under the three different loading paths can generally be performed using a nonlinear least square method (NLSM). Here, the Levenberg-Marquardt NLSM optimization algorithm [42,43] is employed to find the optimal fitting parameter set. Finally, the hardening behavior was defined in terms of uniaxial compression yield stress versus corresponding logarithmic plastic strain. In order to get the experimental uniaxial compression curve, uniaxial compression tests were carried out (see Fig. 5). Nominal stresses and strains were transformed into true stresses and logarithmic plastic strains, which were used as input data in Eq. (5). In Eq. (5) the material hardens only with compressive pressure (the ellipse grows only in the positive pressure direction).

$$p_c = \frac{\sigma_c(\epsilon^{pl}_{axial})[\sigma_c(\epsilon^{pl}_{axial})(\frac{1}{\alpha^2} + \frac{1}{9}) + \frac{p_t}{3}]}{p_t + \frac{\sigma_c(\epsilon^{pl}_{axial})}{3}} \tag{5}$$

4.2. A yield surface with built-in build direction and size effect dependency

Struts in AMLS may take on several geometries and are often not oriented parallel to the build direction. Because the solidification process is geometry-dependent, the formation of microstructural features,

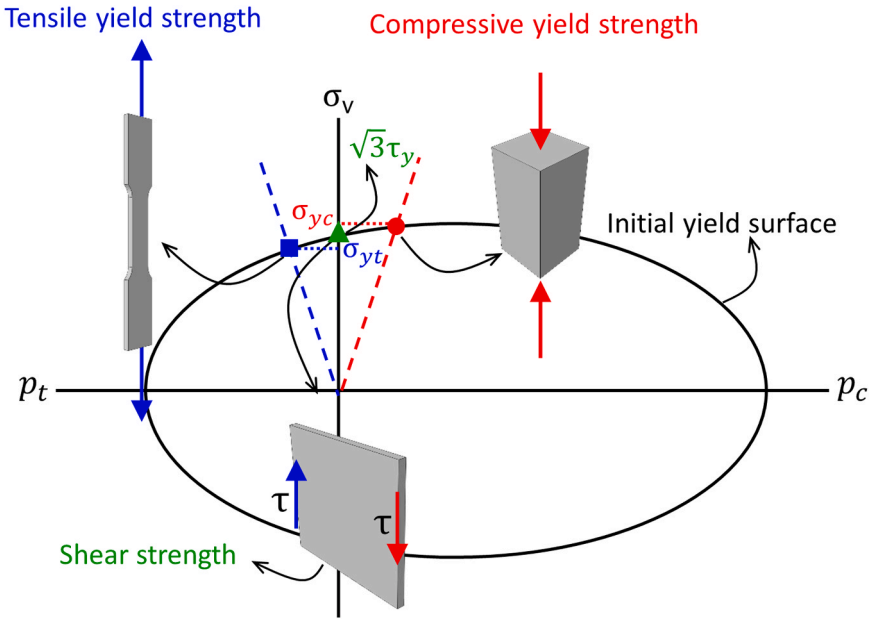

Fig. 4. The schematic of the initial yield surface (the ellipse) indicating yield strength in tension (blue square), yield strength in compression (red circle), and shear strength (green triangle).

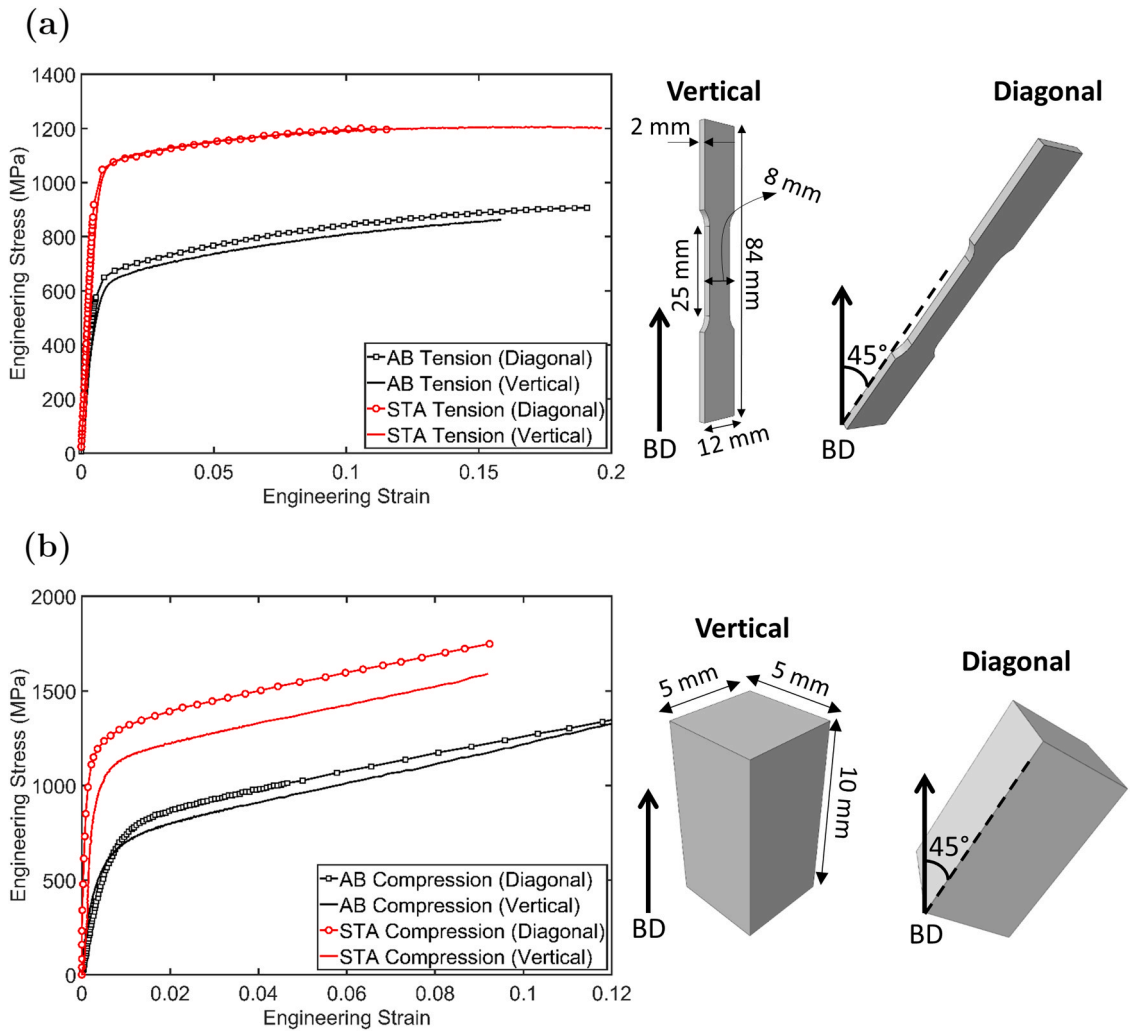

Fig. 5. (a) Stress-strain response of AB and STA bulk IN718 with two different build directions, vertical and diagonal, under quasi-static tension loading, (b) Stress-strain response of AB and STA bulk IN718 with two different build directions, vertical and diagonal, under quasi-static compression loading. The build direction arrow indicates the direction in which layers of building material were stacked during the build process.

including grain size and orientation, porosity size and distribution, and surface roughness, is geometry-dependent. This suggests that mechanical behavior could be affected by the build direction and the thickness of the struts. However, neither the effect of build direction of the struts nor the effects of thin-section behavior on the mechanical properties were accounted for in the MVHM recently developed by the authors [40] and described in Section 4.1. The importance of accounting for build direction and size effects in establishing the initial yield surface is demonstrated in Sections 4.2.1 and 4.2.2, respectively. Additionally, it is essential to note that the effect of these microstructural features on mechanical behavior is dependent on the state of stress (e.g., tension, compression) [40]. Therefore, developing a high-fidelity yield locus to calculate the magnitude of the local stresses under global loading should account for:

1. Effect of the strut build direction on mechanical behavior.
2. Intrinsic size effects.

Furthermore, the evolution of the yield surface should follow the hardening and softening of the struts at different stages of deformation in accordance with the material response to the instantaneous state of local stresses.

4.2.1. *Build direction effect*

Initial microstructural features, response to heat-treatment processes, and ultimately, mechanical behavior of AM structures may vary as the build direction (BD) varies. In order to investigate and incorporate the effects of the build direction on quasi-static tension and compression behavior, mechanical tests were performed on AB and STA IN718 samples fabricated with vertical (test specimens oriented in Z direction or 0˚) and diagonal (test specimens built on a 45˚ angle) orientations with respect to the loading direction, as shown in Fig. 5. Complete details on the build process and mechanical testing are given in Section 3. The effect of solution treatment and aging on the mechanical behavior (yield strength, ultimate tensile strength, and elongation) of vertical and diagonal AM IN718 samples is presented in Table 3. Fig. 5a and Table 3

Table 3
Mechanical properties of AB and STA IN718 under quasi-static compressive and tensile loading.

Mechanical Properties	AB (V)	AB (D)	STA (V)	STA (D)
0.2% Yield Strength (Compression)	644 MPa	742 MPa	974 MPa	1215 MPa
0.2% Yield Strength (Tension)	587 MPa	630 MPa	1048 MPa	1048 MPa
Tensile Strength	863 MPa	908 MPa	1206 MPa	1206 MPa
Elongation	16%	19%	19.5%	12%

demonstrate that diagonal samples in the AB condition have approximately 6% higher tensile yield strengths and plastic flow stress than the vertical samples. In contrast, strength is unaffected by the build direction for STA samples. The most notable difference between the build directions for specimens in the STA condition is the ductility. The elongation to failure in STA diagonal sample is around 12%, which is 38% lower than the vertical sample. The difference between the elongation of struts of different build orientations is substantial because ductility plays a vital role in the deformation mechanisms of AMLS (see Section 7). Fig. 5b and Table 3 demonstrate that diagonal specimens in both heat treatment conditions exhibit 15%–25% higher compressive yield strengths than vertical specimens under quasi-static compression.

The effect of build direction on mechanical properties is critical in LS, as lattice structures consist of many struts oriented at a variety of angles with respect to the build axis. Fig. 6 shows two different lattice structure topologies, OT and RD. Fig. 6a shows 67% of the struts in the OT LS are oriented at a 45° angle with respect to the build direction, with the remainder oriented perpendicular to the build direction. Fig. 6b shows that all struts in the RD LS are oriented at a 54.86° with respect to the build direction. Because the majority of the struts in both topologies are oriented diagonally, the mechanical properties of the diagonally-oriented bulk test specimens are used in the development of the yield surface.

4.2.2. Size effects

Using material properties obtained from testing relatively thick full-size specimens when modeling sub-size AM parts such as thin-wall structures and struts in AMLS is an oversimplification that can lead to an inaccurate representation of the actual mechanical behavior. Recent studies have investigated the geometric size effects on the mechanical properties of different AM alloys including titanium-6% aluminium-4% vanadium [44], 316 L stainless steel [45], and copper-4%chromium-2% niobium [46]. These studies show that the plastic flow stress in AM specimens reduces with sample thickness even when the grain size is unchanged. Reduction in average plastic flow stress is attributed to stress concentrations caused by an increased surface roughness to volume ratio [45], or increased porosity [46] in thin-wall specimens; these properties are dependent upon build parameters [47–49], which vary from material to material. A specific investigation into the porosity and surface roughness of the tensile specimens is beyond the scope of this study; however, in order to demonstrate the effect of wall thickness on mechanical properties of the AM IN718 specimens in this study, dog-bone tensile samples were fabricated with thicknesses of 2 mm and 5 mm, as shown in Fig. 7. All sample thicknesses used a diagonal (45°) build direction. As the stress-strain curve in Fig. 7 demonstrates, the 5 mm samples have higher yield strength and flow stress in both heat treatment conditions. The yield strength in 5 mm AB and STA samples is 12% and 5% higher than each of the 2 mm counterparts, respectively.

5. Material model validation

The discussion presented in Sections 4.2.1 and 4.2.2 underscores the significance of incorporating accurate material properties in modeling the initial yield surface, its evolution, and subsequently the magnitude of the calculated local stresses. Fig. 8 shows the generated yield surface for three different sets of AB samples. The dashed line ellipse represents the yield surface for vertical thin samples (0° build direction and 2 mm thickness), the solid line ellipse represents the yield surface for diagonal thin samples (45° build direction and 2 mm thickness), and the dotted line ellipse demonstrates the yield surface for thick diagonal samples (45° build direction and 5 mm thickness). Fig. 8 shows there is a considerable difference between these three yield surfaces. Therefore, a constitutive model with appropriate yield criteria for different material properties must be used to accurately predict a strut's local stress state and predict its role in global mechanical behavior.

The compressive, tensile, and shear yield strengths of the diagonal thin specimens used to define the yield surface for all modeling analysis are taken from Fig. 5 presented in Section 4.2. In addition, these three points are measured for all heat-treatment conditions (microstructures) from Section 3.2. Once these strengths are defined, a unique elliptical yield surface can be generated without a need to perform hydrostatic compression/tension tests. After the yield surface is obtained for AB and STA microstructures (see Fig. 9), the numerical simulation for local stress analysis is conducted with the commercial FE package Abaqus/Explicit. The results are then validated with the experimental results (see Section 6.1).

6. Modeling and material parameters

In this study, all specimens have four unit cells (each $4 \times 4 \times 4\ mm^3$) in each direction, yielding an overall structure $16 \times 16 \times 16\ mm^3$. Each topology considered has a relative density (ρ^*, defined as the ratio of the LS density to the building material density) of 30%. Stretching dominated and bending dominated structures (as determined by Maxwell's criterion [50]) or softening-based and hardening-based structures [40] were chosen for this analysis; OT is a stretching-dominated (softening-based) structure, and RD is a bending-dominated (hardening-based) structure.

Following the model validation in Section 5 and creation of the initial yield surface (Fig. 9) to allow the application of the MVHM, CAD

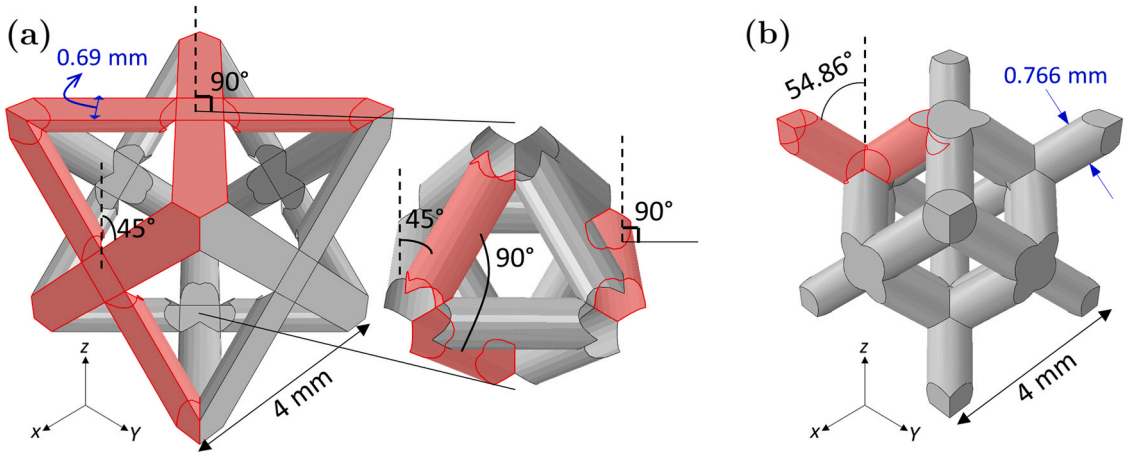

Fig. 6. (a) Octet truss LS topology with 45° and 90° struts angle, (b) Rhombic dodecahedron LS topology with 54.86° strut's angle. The relative density of both topologies is 30%.

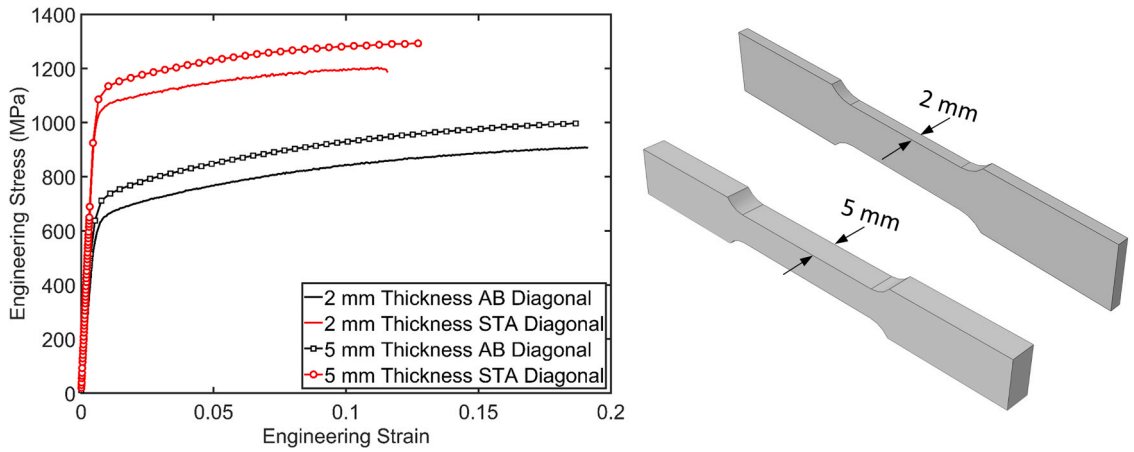

Fig. 7. Size effect (2 mm and 5 mm thickness) sensitivity of bulk IN718 dog-bone samples. Specimens were manufactured diagonally with regard to build direction.

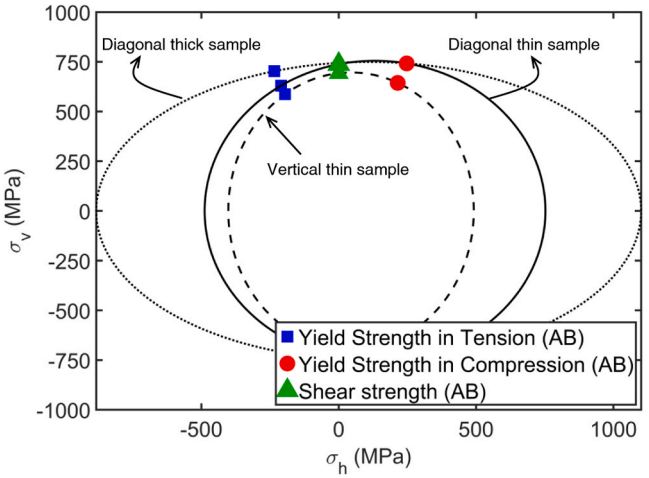

Fig. 8. The comparison between the generated yield surface from the AB diagonal thin sample (dashed line), AB vertical thin sample (solid line), and AB diagonal thick sample (dotted line).

models for each lattice structure were created and imported into the finite element package ABAQUS [51]. The models were meshed using 4-node linear tetrahedral elements (C3D4). Subsequently, moving and fixed rigid plates were defined at the top and bottom of the LS model, respectively, as demonstrated in Fig. 10. The frictional contact

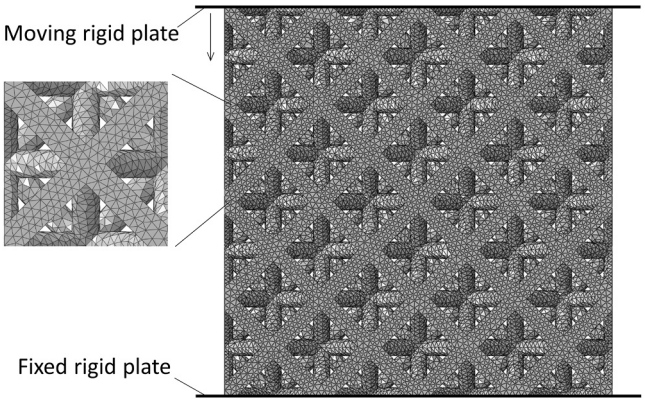

Fig. 10. The quasi-static compression simulation boundary condition used for OT LS. The top plate is moving freely in the loading direction, and the bottom plate is fixed. This exact boundary condition was applied to all other topologies.

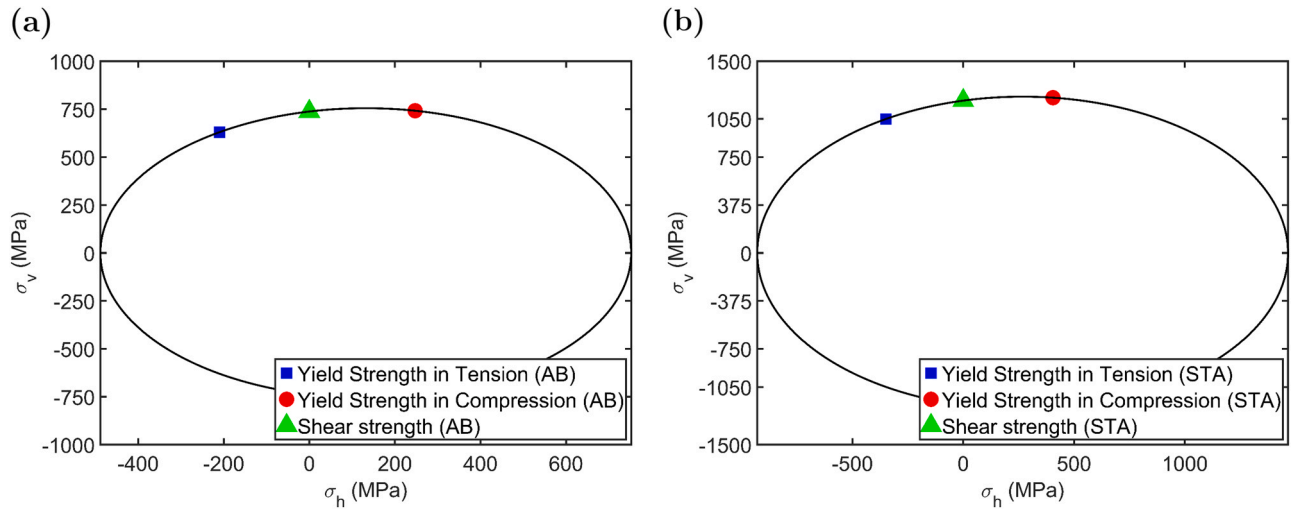

Fig. 9. The schematic of the initial yield surface (the ellipse) indicating yield strength in tension (blue square), yield strength in compression (red circle), and shear strength (green triangle) for the (a) AB and (b) STA heat-treatment conditions.

coefficient between the rigid plates and the LS was set to 0.2. A general contact algorithm was applied to the model to account for the contact between the struts during deformation. Loading was prescribed by applying a total displacement of 4.8 mm to the movable rigid plate at a constant strain rate of 0.1 s^{-1}. The deformation of the LS was then analyzed in three dimensions using an explicit algorithm.

Failure analysis was performed based on damage initiation and evolution criteria for ductile metals. The damage initiation criterion used in this work is based on the Johnson-Cook damage model defined in Eq. (6) [52].

$$\bar{\epsilon}_D^{pl} = [D_1 + D_2 exp(-D_3\eta)][1 + D_4 ln\dot{\epsilon}*][1 + D_5 T*] \quad (6)$$

where $\bar{\epsilon}_D^{pl}$ is the equivalent strain to fracture. Stress triaxiality is defined as $\eta = \sigma_m/\bar{\sigma}$, where σ_m is hydrostatic pressure stress and $\bar{\sigma}$ is the von Mises equivalent stress. $\dot{\epsilon}* = \dot{\bar{\epsilon}}^{pl}/\dot{\epsilon}_0$ is the non-dimensional plastic strain rate, and T^* is the dimensionless temperature. D_1, D_2, D_3, D_4, and D_5 are material dependent fracture constants, which were acquired by fitting the experimental results as detailed in Table 4. The data in Table 4 is consistent with that used for the quasi-static compression simulation of all LS topologies for AB and STA conditions.

Upon reaching the damage initiation criterion, a damage evolution can be defined for which the true stress is reduced to zero while the true strain continues to increase. The damage evolution decreases the stiffness of the element as the plastic strain continues to increase past the strain value of the damage initiation criterion and removes the element from the mesh when the stiffness is reduced to a factor of 0.001 that of the initial stiffness (99.9% reduction of the stiffness). The damage evolution law employed was based on Hillerborg's fracture energy principle [53], which assists in avoiding mesh-dependency in the results of the failure analysis, particularly with regard to energy dissipation due to strain localization. Moreover, a mesh convergence analysis was conducted to find a balance between computation time and stability in the stress distribution when the mesh size is altered to prevent mesh dependency further. A global mesh size of 0.2 mm was found to be sufficient for all four topologies considered in this study. To further reduce run times and increase the time steps of the simulation, a mass scaling process was performed by artificially increasing the density of the material. To ensure that accuracy of the results was not affected by the mass scaling technique, kinetic energy was monitored during the simulation to ensure that it remained less than 2% of the total internal energy during the deformation process, and critical results from simulations with different mass scaling magnitudes were compared to quantify the mass scaling effects.

6.1. Numerical model validation using experimental data

To verify the accuracy of the modified volumetric hardening model (MVHM), the global behavior of both OT and RD LS, including the quasi-static compressive stress-strain relationships, were calculated using an FE solver and compared with experimental results. Since the primary goal is to understand the deformation and failure mechanisms of both OT and RD topologies after yielding, specifically the sharp drop in flow stress occurring between 10% and 30% strain, the results are calculated and presented up to 30% strain. Fig. 11a–d compare the stress-strain curves obtained from experiments and MVHM for AB octet truss, AB rhombic dodecahedron, STA octet truss, and STA rhombic dodecahedron, respectively. In Fig. 11, the blue and black lines indicate the two series of experimental results plotted against the numerical results with the red line. Fig. 11 suggests that the MVHM results are in good agreement with the experimental results. Since the developed MVHM follows the experimental measurements closely, it provides an opportunity to perform accurate stress analysis at the strut level to explain the deformation and failure mechanisms of OT and RD topology AMLS.

Table 4
AB and STA IN718 damage parameters of the Johnson-Cook damage criterion model used for the simulations.

Heat-treatment	D_1	D_2	D_3	D_4	D_5	Displacement at failure
AB	0.05	0.15	-1.2	0.002	0.46	0.2
STA	0.03	0.2	-1.45	0.002	0.46	0.09

7. Numerical and experimental study on the deformation mechanisms of OT and RD topologies

To understand the specific roles of microstructure and topology on mechanical behavior, the information about underlying deformation mechanisms at different stages of deformation is coupled with the local state of stress. The obtained information is used to design and build new topologies. Moreover, as demonstrated in Section 2, the goal is to take advantage of the increased yield strength of solution treated and aged specimens. Therefore, local stress analysis and deformation mechanism investigation is only conducted for the STA heat-treatment condition to understand the mechanisms responsible for the macroscopic flow stress drop and use the knowledge of the deformation mechanisms to mitigate the identified drop by designing new unit cell topologies. Local instability analysis relies on considering the number of elements (material points) in tension (NET), the number of elements in compression (NEC), and the total number of the elements both in tension and compression (NET+NEC). For instance, if the volume of an element increases from the n^{th} increment to the $(n+1)^{th}$ increment, the examined element is under tensile loading in the $(n+1)^{th}$ increment. Those elements with the volume change of zero or near zero (i.e., $\Delta V = 0$) are not considered in the results. A $\Delta V = 0$ means either a non-zero deviatoric state of stress or the element volume is changing less than 0.01% and can be excluded from the calculation. The complete description of this classification is presented in [40].

The status of materials points under tension or compression could further be linked to local damage initiation. Sections 7.1 and 7.2 use this approach to investigate the causes for the drop in the stress value of STA heat-treated AMLS with OT and RD topologies. In the wake of such analysis, new topologies with the same relative density as OT and RD are introduced to mitigate local damage and instabilities. The discussion for new topologies and their performance are presented in Sections 8.1 and 8.2.

7.1. Octet truss topology

In order to explain the deformation and failure mechanisms of OT topology AMLS, NET, and NEC as a percentage of the total number of elements and the correlation between the global behavior (engineering stress-strain) and the state of stress that each material point experiences at different strain increments are established via MVHM (see Fig. 12a). Furthermore, the total number of failed elements (TNFE) in each increment is calculated and separated into the number of failed elements under tension (NFET) and the number of failed elements under compression (NFEC) (see Fig. 12b). Finally, to validate the results and further elaborate on the deformation and failure mechanisms, a comparison between the experimental and simulated (MVHM) deformation mechanisms have been made at three different strain increments: 0%, 15%, and 18%. The strain values of 15% and 18% correspond to the maximum values of TNFE. Additionally, the damage initiation and evolution for those three strain values are demonstrated in a 3D view by singling out a unit cell from the simulation analysis. The unit cell was chosen from the area in which damage was initiated following the Johnson-Cook damage initiation criterion (JCCRT). The color contour indicates the locations of damage; the red areas with higher JCCRT values are located between the horizontal struts, which are under a tensile state of stress (see Fig. 12a), and nodes. It should be pointed out

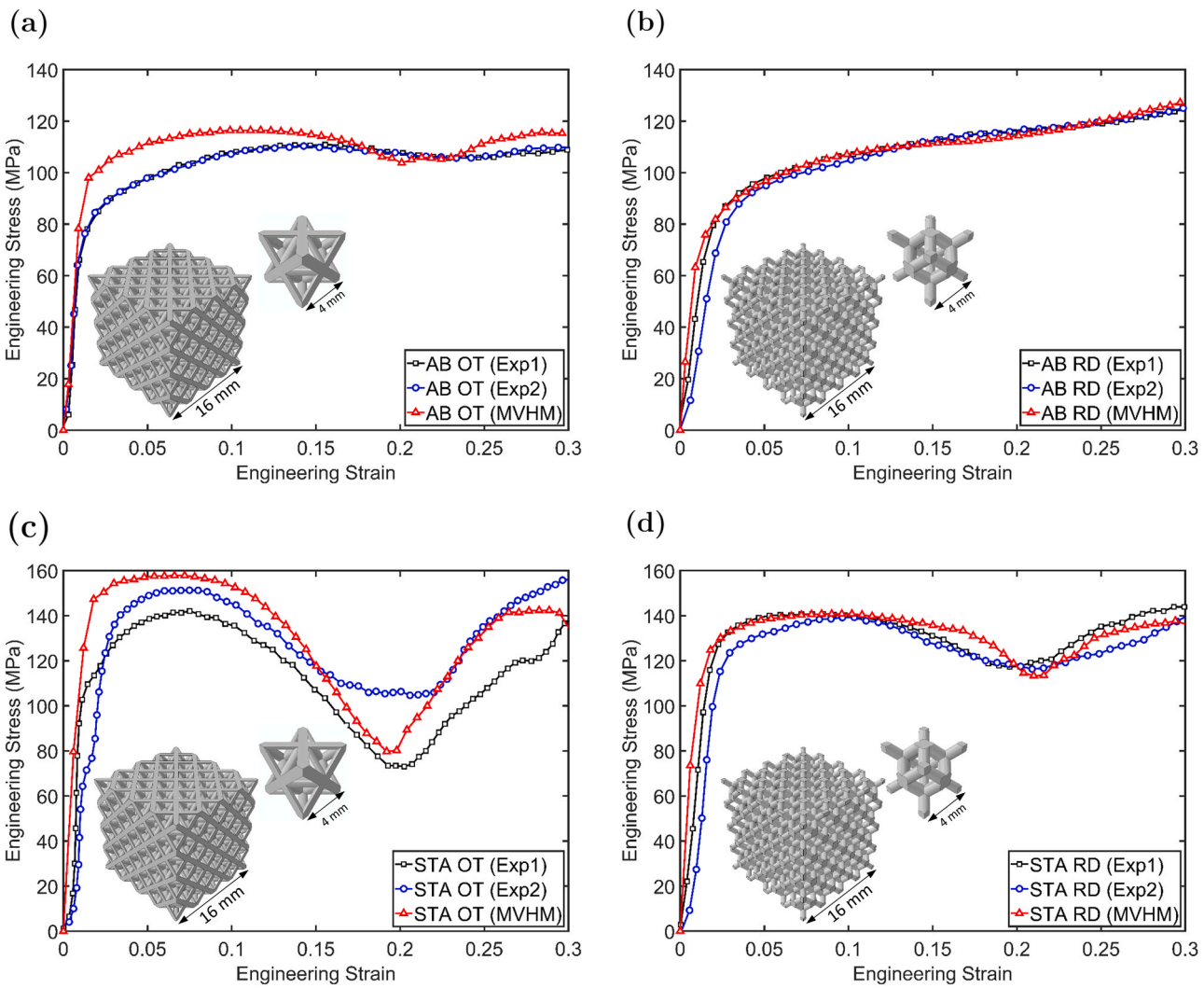

Fig. 11. Experimental and numerical comparison of quasi-static behavior of AMLS made of IN718, with 4 mm unit cell size, and fixed topology and microstructure: (a) AB Octet truss; (b) AB Rhombic dodecahedron; (c) STA Octet truss; (d) STA Rhombic dodecahedron. For each condition, two samples were tested experimentally (black and blue solid lines), and then the numerical analysis were conducted and plotted against the experimental results (red solid line).

that JCCRT equal to or greater than 1 means damage is initiated. With that in mind, the deformation and failure mechanisms of OT are explained in detail as follows by using the stress-strain curve (Fig. 12a) of the OT topology that entails elastic, yielding, and post-yielding regimes up to 30% strain.

Around 10% strain, plastic flow stress begins to drop gradually, and around 20% strain has dropped by approximately 50%. This area is called the failure zone. By looking at Fig. 12c–e, it can be observed that this failure zone coincides with the formation of a structural shear band. In the failure zone area (see Fig. 12a), NET is increasing, and it reaches its maximum value (22%) in the global stress-strain valley (at around 20% strain), while NEC is decreasing and reaches its minimum value (15%). On the other hand, the total number of elements involved in the deformation (NET+NEC) is decreased from 60% to 37% in the flow stress drop. Therefore, it can be inferred that around 60% of the elements involved in the deformation is under a tensile state of stress between 15%–20% global strain. Fig. 12b demonstrates that elements in tension govern the deformation mechanisms in the failure zone and cause the structural shear band by investigating and comparing the elements that failed under tensile and compressive states of stress. Fig. 12b demonstrates that in the failure zone, NFET is considerably higher than NFEC. For example, at around 18% strain, NFET is three times larger than NFEC. Overall, from Fig. 12b, it can be noted that more than 50% of the TNFE failed under tension.

At this point, the question to ask is why material points under tension are dominating failure? To answer this question, first, it should be pointed out that in general, in any AMLS, regardless of topology, 10–30% of the elements go under tension when the entire AMLS is subjected to quasi-static uniaxial compression loading. While 10–30% of elements in tension seem to be minor, these elements can lead to local instability and premature failure. Additionally, due to the strength differential effect in bulk STA IN718 [54], yield strength in compression is 16% higher than yield strength in tension. Furthermore, the elongation at failure in bulk STA IN718 is only about 12% (see Table 3). As a result, struts are more likely to fail at a lower value of stress or elongation when subjected to tensile loading compared to the struts subjected to compressive loading. Both experiments and simulation (see Fig. 12c–e) illustrate that horizontal struts (see blue struts in the unit cell in Fig. 12a) are tension-dominated struts. Based on JCCRT local contour plot (see Fig. 12c–e), horizontal struts have a higher value of JCCRT, which indicates an area with localized plastic strain. In other words, horizontal struts undergo tensile stress, then fracture, causing the structural shear bands.

7.1.1. Lessons learned from deformation mechanisms of OT topology

Analyzing the deformation and failure mechanisms of STA OT AMLS

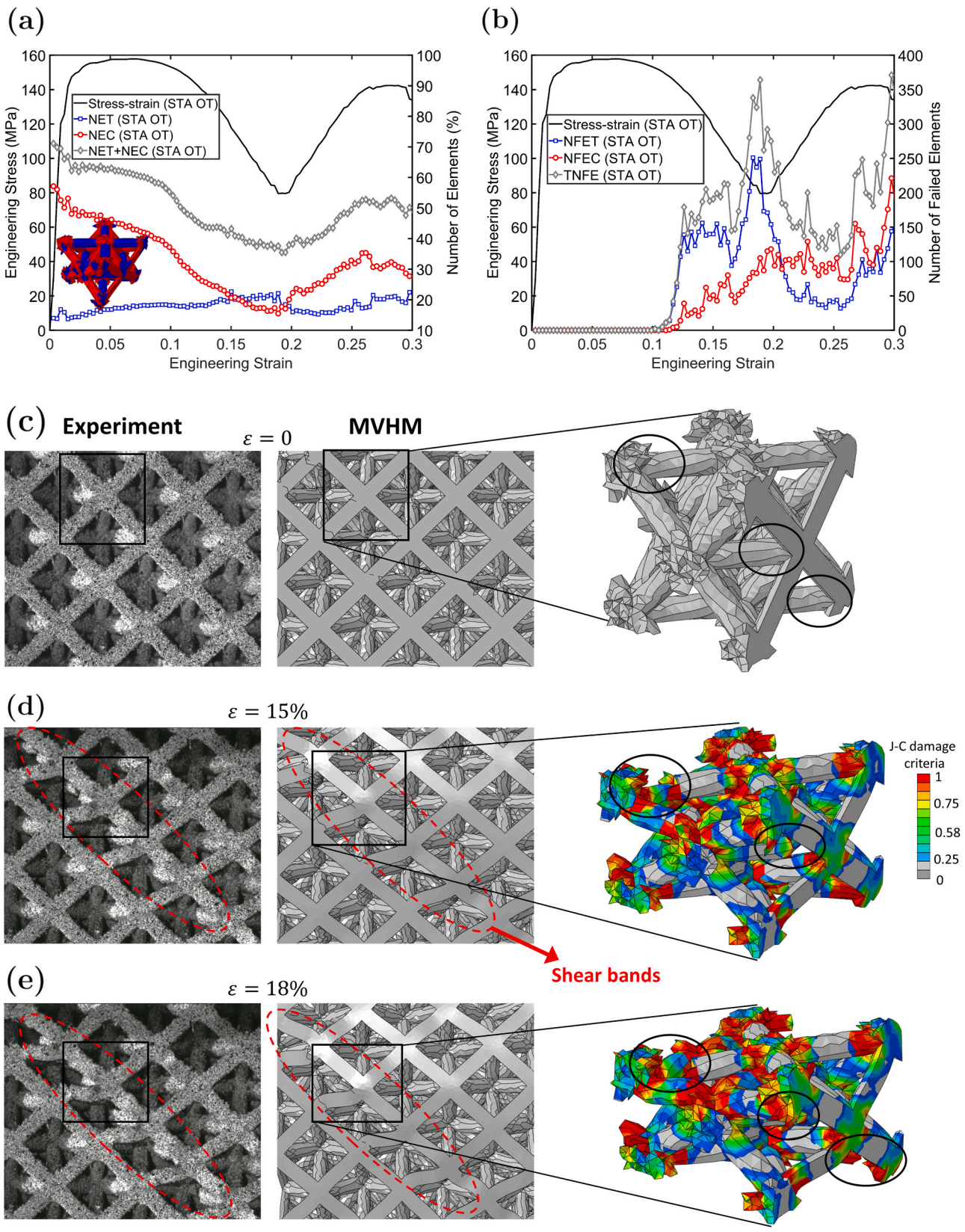

Fig. 12. Octet truss topology under quasi-static compression loading (a) engineering stress, NET, NEC, and NET+NEC are plotted against the engineering strain, and (b) the number of failed elements NFET, NFEC, and TNFE in each increment is plotted vs. strain. Deformation mode mechanism comparison between experiment and MVHM for three different strain values is shown in (c), (d), and (e). One unit cell is singled out to show the Johnson-Cook contour plot of OT topology during deformation. It is seen that damage initiates first in horizontal struts (having angles of 90° with build direction), going under a tensile state of stress. The red dashed-line indicates the location of shear bands.

gives valuable insight regarding the drop in the flow stress, and particularly the structural shear band formation, which can be used as guidelines to create a new optimized topology that overcomes the flow stress drop stemming from the microstructural shortcomings (i.e., the reduced elongation to failure). Guidelines for developing a new topology can be generalized as follows:

1. A higher NET increases the likelihood of local tensile fracturing and shear band occurrence in AMLS.
2. A lower value of NET+NEC during deformation means increasing the possibility of plastic strain and damage localization.
3. AMLS with horizontal struts have higher NET and higher tension-based elongation, and as a result are more prone to fracture.

To prevent the flow stress drop, a topology with higher NEC and NEC+NET is desirable. More NEC and NET+NEC implies that more nodes and struts are involved in the deformation, resulting in less localization. With more NEC and NET+NEC, the structural shear bands can be minimized, and more homogeneous deformation could occur, thus higher energy absorption capacity. To achieve this goal, first, the new topology should have less or no horizontal struts for two main reasons: (i) horizontal struts are weaker than diagonal struts from a manufacturing perspective [55], (ii) horizontal struts mostly undergo a tensile state of stress and therefore are more prone to fracture. The diagonal struts in the new AMLS should be designed so that the elongation in struts and nodes is less than 10% to prevent fracture under tension.

7.2. Rhombic dodecahedron topology

Compared to the OT topology, in RD, the minimum stress value that the flow stress drops to during the global stress-strain valley is 60% higher than its counterpart in OT. This observation implies the importance of topology in the deformation behavior of AMLS. Moreover, the NET has an abrupt change around 18% strain when the drop occurs, and it reaches its maximum value of 22%. Therefore, it can be inferred that the tensile state of stress induces damage and softening behavior in RD as well. Fig. 13a shows that NET+NEC decreases from 5% to 22% strain. This portion of the stress-strain curve can be broken into two separate regions. First, examine the part of the curve that falls between 5%−15% strain. In this region, the reduction in NET+NEC coincides with plastic strain localization. This can be further verified by exploring the corresponding number of failed elements in Fig. 13b, as the number of failed elements in this deformation range is negligible. When deformation proceeds from 15% to 22%, strain reduction in NET+NEC coincides with damage localization instead of plastic strain localization. Furthermore, between 5%−18% strain, NET is almost constant (20%), but it increases slightly from 18% to 22% strain, and at 22% strain, is equal with the NEC. This is associated with the failure zone when the plastic flow stress drop occurs.

In this area, NET and NEC are almost equal; NFET and NFEC are approximately the same as well. Comparing the failure zone of RD with OT demonstrates the significance of topology in controlling the influence of the microstructure since both topologies have the same relative density (30%) with the same microstructure induced by STA heat-treatment.

Although the NET and NEC in the failure zone are almost the same (≈ 20%), the tensile loading is still the primary reason for the unexpected softening. Looking at the unit cell in Fig. 13c−e, it can be seen that nodes have the highest value of JCCRT, and the unit cell in Fig. 13a displays that the nodes are dominated by the tensile state of stress (blue color). Moreover, in Fig. 13c−e, both experiment and the simulation illustrate the damage initiation and evolution in the joints. When RD is under quasi-static compressive loading, struts (see two red color struts in Fig. 6b or blue spot on the unit cell in Fig. 13a) primarily undergo bending, and with increased bending get disjointed by the tensile state of stress from their original anchor nodes. The question to ask here is why NET and NEC are almost equal in the failure zone? As noted, struts are primarily in bending, and since in bending, the compressive and tensile normal stresses are almost balanced (to give a zero net horizontal force), NET and NEC are almost the same. However, considering STA IN718 has lower yield strength in tension than the compression, the possibility of material points under tension, causing damage, and governing the failure zone is higher.

7.2.1. Lessons learned from deformation mechanisms of RD topology

The deformation and failure mechanisms of RD verify the relationship between microstructural and topological effects on the mechanical performance of AMLS. The results (see Fig. 13a−e) show that the RD topology has better compatibility with STA microstructure than the OT topology. This results in improved mechanical properties such as higher energy absorption capacity (≈ 16% more than OT) and reduced flow stress drop (≈ 60% improvement). Moreover, there are no horizontal struts in RD topology, although this has not reduced the NET compared to OT. With no horizontal struts (which have lower strength than diagonal struts), the NFET is reduced, suggesting that material points under tension are not as detrimental to RD AMLS as in OT AMLS. Note that NET in OT and RD are almost the same (around 20%), and the only significant difference is related to NEC. The change in NEC in RD (≈ 20%) is much smaller than in OT (≈ 50%); the increased number of total elements involved in the deformation may contribute to why no structural shear bands are seen in the RD topology. Additionally, material points in the struts and nodes under tension do not experience elongation past the fracture point (≈ 12%) in the RD topology, further preventing localization such as shear bands. The main drawback to the deformation mechanisms of RD is the tensile stress concentrations at the nodes, which could lead to node fracture and instability in the structure. The lessons from deformation and failure mechanisms of RD can be outlined as follows:

1. Having diagonal struts does not guarantee reduction in NET, but since diagonal struts have higher yield strength than the horizontal and vertical struts, they are preferable from a manufacturing perspective.
2. In diagonal-strut-based structures such as RD, nodes are the primary mode for accommodating plastic strain, which in turn enhances the probability of damage localization and node fracture.

Therefore, one effective way to prevent plastic strain localization, which results in damage initiation is to increase NEC and NET+NEC through imposing boundary conditions such as a bracing system to support the nodes and struts to prevent these elements from exceeding the elongation to fracture. For example, bracing systems are integral parts of most bridge structures to improve lateral and longitudinal stability. The goal of adding additional bracing to AMLS is to distribute the vertical bending effects between the struts, and to ensure that the applied loadings are shared between all the struts and nodes, hindering localization.

8. Transformation of knowledge to design new topologies

Lessons learned from the mechanical behavior of OT and RD topologies presented in Sections 7.1 and 7.2 are used to design two new topologies. The design strategy of the new topologies results in improved performance: 24–53% increases in energy absorption compared to OT and RD topologies, as detailed in Sections 8.1 and 8.2.

8.1. Rhoctet topology

The rhoctet (RT) design relies on confining the struts and nodes which undergo tensile states of stress. This is done by increasing NEC and therefore preventing strut and node elongation from exceeding 10%. As a result, RT demonstrates 27% and 10% higher energy

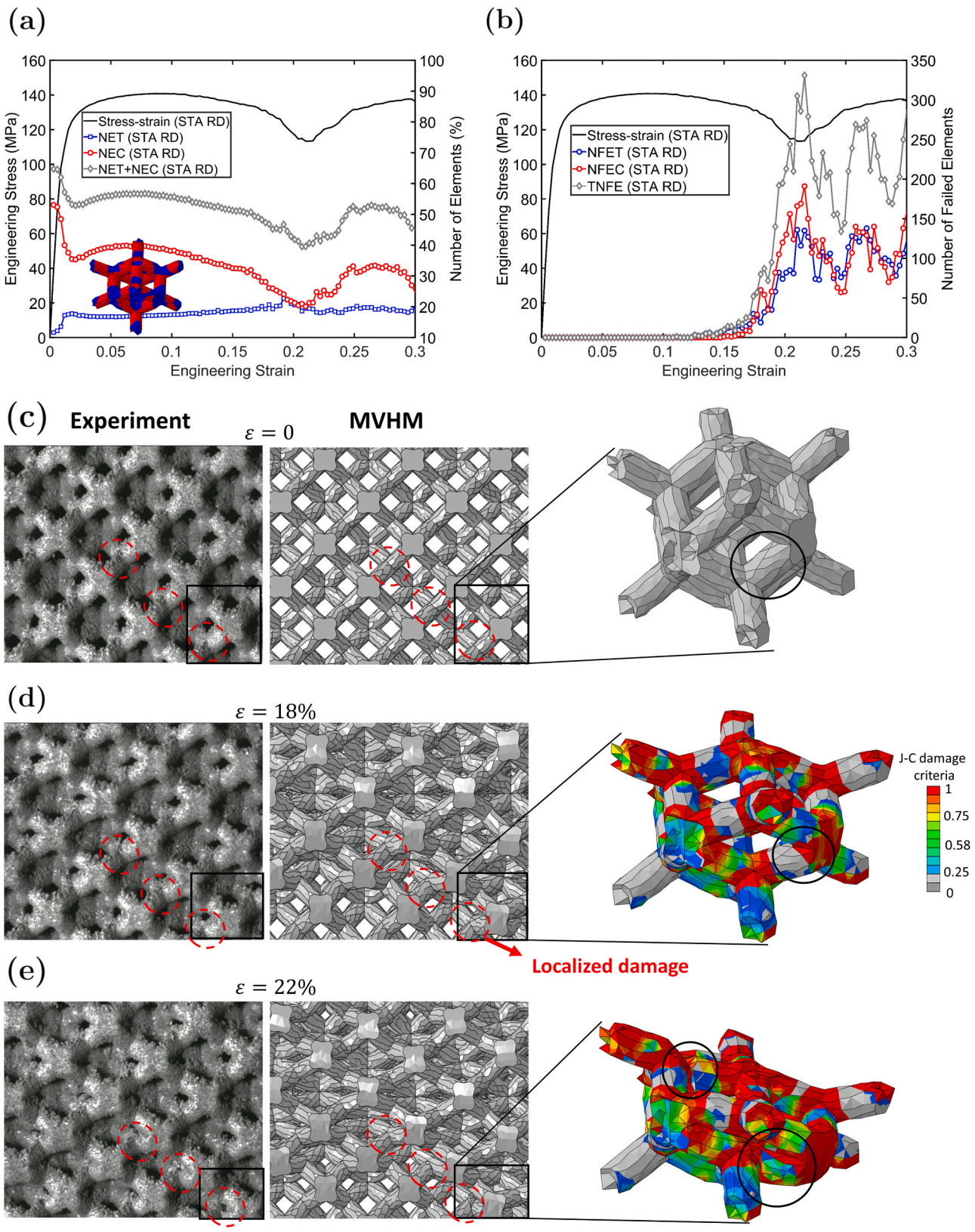

Fig. 13. Rhombic dodecahedron topology under quasi-static compression loading (a) engineering stress, NET, NEC, and NET+NEC are plotted against the engineering strain, and (b) the number of failed elements NFET, NFEC, and TNFE in each increment is plotted vs. strain. Deformation mode mechanism comparison between experiment and MVHM for three different strain values is shown in (c), (d), and (e). One unit cell is singled out to show the Johnson-Cook contour plot of OT topology during deformation. It is seen that damage initiates first in the joints, going under a compressive state of stress. The red dashed-line indicates the location of the damage.

absorption capacity compared to OT and RD topologies, respectively. Furthermore, the RT topology has an 82% and 50% improvement in the flow stress drop compared to OT and RD, respectively (see Fig. 14). To explain this mechanism in more detail, local property analysis including NET, NEC, NET+NEC (see Fig. 15a), and failure analysis (see Fig. 15b) were conducted. In addition, the deformation modes of RT from experiments and simulation are compared and a JCCRT contour plot is used to display the localized damage areas (see Fig. 15c–e) in conjunction with the plastic stress flow. The results indicates up to 75% increase in NET+NEC and up to 50% increase in NEC compared to OT and RD topologies.

Fig. 15a illustrates that the NET+NEC is almost constant, around 70% of the total number of elements in the structure. That means the large number of struts and nodes are involved in the deformation, and the applied loading is distributed more uniformly than the OT and RD topologies. Fig. 15a also shows that NET and NEC lie between 20% and 30%, and 30% and 40%, respectively. This indicates, there is no significant change in either NET and NEC throughout the deformation process, as compared to OT and RD topologies. As a result, RT does not show strain localization and damage (see Fig. 15c–e).

NET in RT is approximately 6% higher than NET in OT and RD throughout the entire deformation. However, in RT, material points under tension are no longer governing the deformation and failure process (see Fig. 15b). Fig. 15b demonstrates that less than 20% of the total failed element failed under the tensile state of stress. The reason is that the provided support by adjacent struts hinders tensile elongation of material points to under 10%. This can be validated by the JCCRT contour plots (see Fig. 15c–e), which display the more uniform distribution of JCCRT in the struts and nodes compared to OT and RD. It is also important to note that the strut diameter in RT is 10% and 20% smaller than the strut's diameter in OT and RD, respectively. Thus, it is reasonable to conclude that thicker struts do not necessarily deliver enhanced mechanical properties such as higher yield strength and higher energy absorption capacity in AMLS, suggesting topology may counteract geometric size effects.

The quasi-static compression behavior of RT exhibits notable improvements in yield strength, plastic flow stress, and energy absorption capacity compared to the OT and RD topologies. The main attribut to this proprties enhancement is the 20% increase in total number of elements involved in the deformation from OT and RD to RT by changing the topology, preventing localization based on the guidelines listed in the Sections 7.1.1 and 7.2.1. The number of horizontal struts in RT topology is minimized. In addition, the local confinement imposed on material points which undergo tension is leveraged as an additional strengthening mechanism.

8.2. Rhoctan topology

The deformation and failure mechanisms of RT indicate that the effect of the STA microstructure can be controlled by changing the topology. In other words, there is a synergistic effect between topology and microstructure. Hence, topology-microstructure-based optimization leads to improved structural integrity in AMLS. On the other hand, maintaining the structural integrity of AMLS after yielding is key to ensuring a longer life span for integral materials in critical applications. The structural integrity, such as damage resistance and vulnerability in RT, was improved compared to OT and RD topologies. While RT demonstrates considerable mechanical behavior improvement compared to OT and RD, the topology-microstructure-based optimization technique approach, which has been presented here, can be used to further enhance RT strength and energy absorption properties. This relies on finding the highest compatibility between topology and underlying strut microstructure. Fig. 16a–c compares the topology and quasi-static compression behavior of OT, RD, and RT with the newly developed topology in this section named Rhoctan (RTN). Evidently, RTN does not show (Fig. 16d) the characteristic drop in flow stress which was previously seen in OT, RD, and to some extent, RT topologies. This improvement is attributed to a 10–60% increase in NET+NEC from OT, RD, and RT to RTN topology (Fig. 16c). Furthermore, the area under the entire stress-strain curve of RTN from Fig. 16d indicates the amount of energy absorbed per unit volume is 53%, 25%, and 15% higher than OT, RD, and RT topologies, respectively. Fig. 16c elucidates the deformation mechanisms of RTN based on MVHM analysis. In RTN, NET (≈ 25%), NEC (≈ 50%), and NET+NEC (≈ 75%) are almost constant as the deformation proceeds, suggesting the absence of damage localization in the structure. In fact, RTN is designed based on the STA microstructural constraints, including low ductility under the tensile loading by:

Fig. 16c elucidates the deformation mechanisms of RTN based on MVHM analysis. In RTN, NET (≈ 25%), NEC (≈ 50%), and NET+NEC (≈ 75%) are almost constant as the deformation proceeds, suggesting the absence of damage localization in the structure. In fact, RTN is designed based on the STA microstructural constraints, including low ductility under the tensile loading by:

1. Minimizing the number of horizontal struts,
2. Imposing local confinement to support nodes to avoid node fracture,
3. Minimizing the space inside of the topology by creating diagonal struts as an obstacle to elongation exceeding 10%.

With the constraints, the struts and nodes are prevented from elongating more than 10% under tensile loading. Furthermore, the

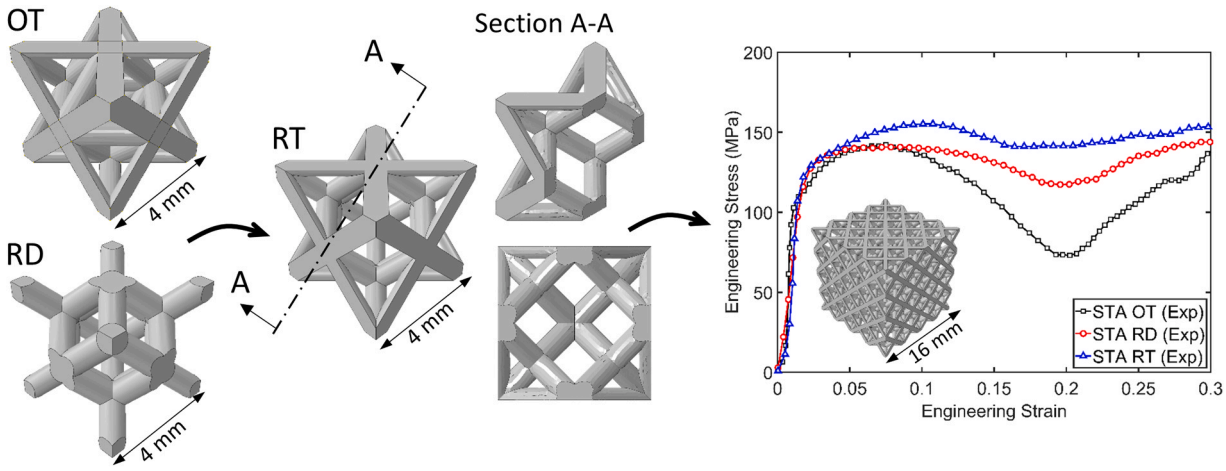

Fig. 14. Considering the deformation mechanisms of OT and RD topologies; RT topology is designed using MVHM model, and then the quasi-static compression behavior of RT is compared with OT and RD experimentally. The results show an improvement in flow stress and energy absorption capacity.

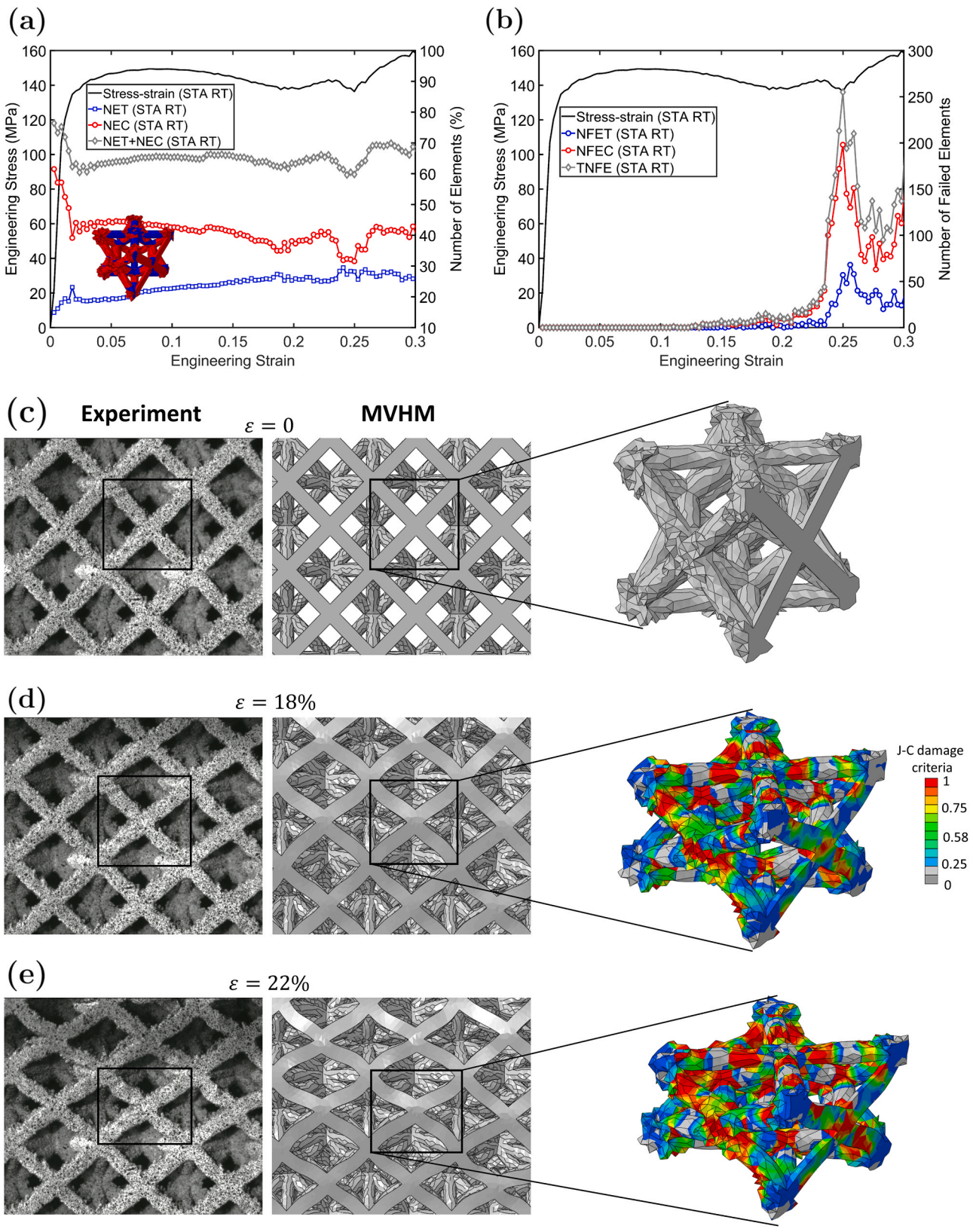

Fig. 15. Rhoctet topology under quasi-static compression loading (a) engineering stress, NET, NEC, and NET+NEC are plotted against the engineering strain, and (b) the number of failed elements NFET, NFEC, and TNFE in each increment are plotted vs. strain. Deformation mode mechanism comparison between experiment and MVHM for three different strain values is shown in (c), (d), and (e). One unit cell is singled out to show the Johnson-Cook contour plot of OT topology during deformation. The deformation mechanisms are smooth and no severe localized damage is noticed.

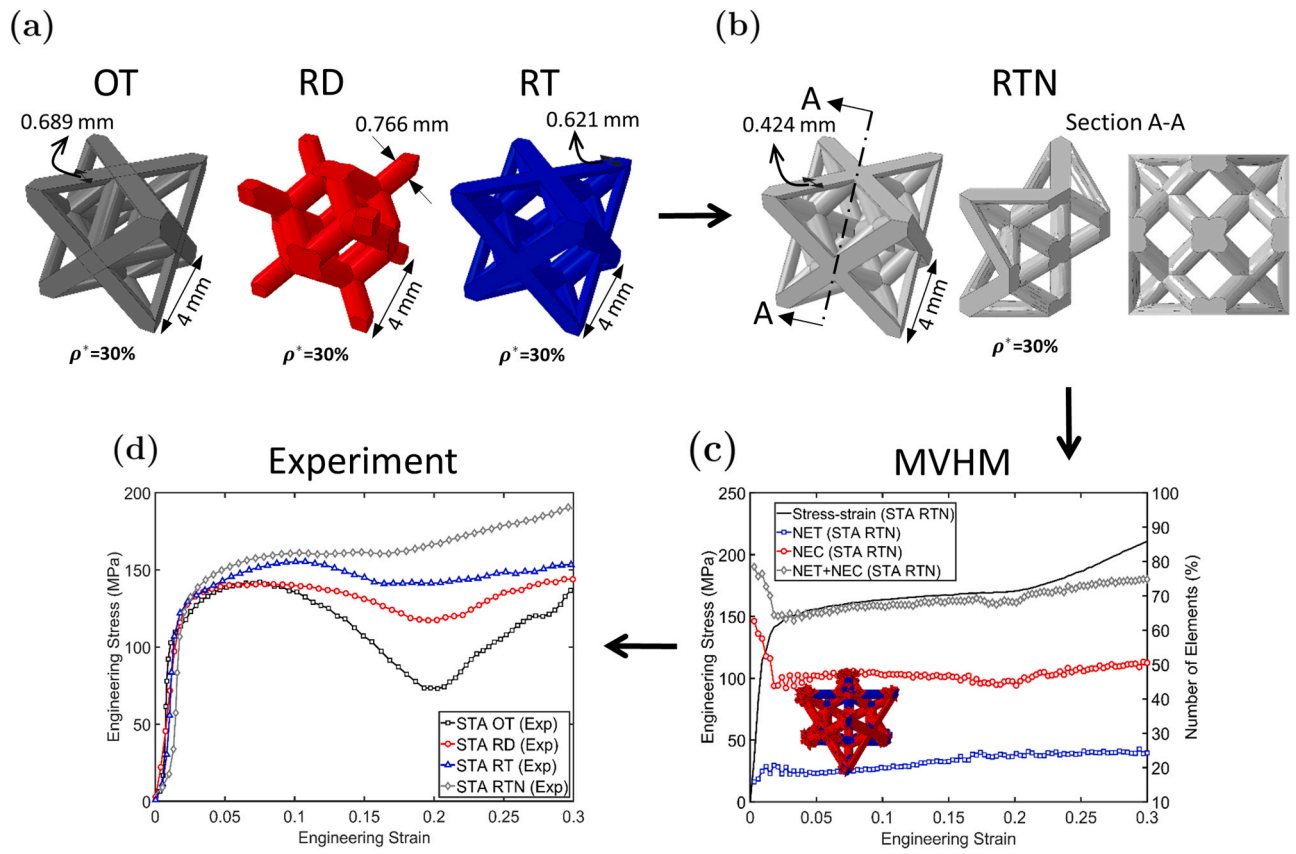

Fig. 16. Introducing RTN topology, which is created based on the deformation mechanisms of STA OT, RD, and RT topologies. (a) OT, RD, and RT unit cell topology, (b) RTN unit cell topology, (c) engineering stress, NET, NEC, and NET+NEC are plotted against the engineering strain to analyze the deformation behavior of RTN as a new optimized topology, (d) the experimental results of quasi-static compression behavior of STA OT, RD, RT, and RTN.

deformation mechanisms change from damaged-based mechanisms to strut self contact-based mechanisms. Finally, it can be inferred from the results that RTN topology can be successfully implemented in several different applications that need high energy absorption capacity and structural integrity under compressive loadings, such as aircraft wings and fuselages, a rocket bodies, and all manners of armor, etc.

In order to compare the energy absorption capacity of RTN topology with other optimized foams and lattice structures made of metals and composite, an Ashby map containing energy absorption per unit volume versus relative density and specific energy absorption per relative density is constructed and presented in Fig. 17a and b). It should be pointed out that to calculate the energy absorption capacity in Fig. 17a and b, the area below the stress-strain curve up to densification is used. To maintain the optimized property-to-weight ratio, only relative densities between 10% are 50% considered in Fig. 17. Therefore, energy absorption capacity values between 90 MJ/m^3 and 500 MJ/m^3 for topologies with 10–40% relative density are marked, with the red color denoting a previously unclaimed area.

Fig. 17a and b suggest that the RTN topology exhibits considerably higher energy absorption capacity compared to other metallic and composite structures used in several other studies. The significance of such an achievement in energy absorption capacity can be explained by an example taken from Fig. 17a and b. To obtain an energy absorption capacity close to the unclaimed area with titanium alloy, the relative density should be increased by approximately 40% (from 30% to almost 42%).

9. Summary

In this study, a topology-microstructure-based optimization technique was developed to generate AMLS topology with the highest compatibility between structural topology and the underlying microstructure. The effectiveness of the proposed optimization approach was examined by substantially increasing yield strength, plastic flow stress, and energy absorption capacity of previously optimized topologies. First, customized yield surfaces (MVHM) for AMLS with AB and STA microstructures with built-in build direction and size effect dependency were assigned to the respective struts to obtain accurate values of local stresses and the hardening and softening of the flow stress curves as deformation proceeds. Once the developed model was validated with experimental data, it was used to elucidate the deformation mechanisms of OT and RD topologies. Then, based on the deformation and failure mechanisms of these two topologies, two new, optimized topologies were generated and validated experimentally: RT and RTN. The generated topologies showed higher yield strength coupled with maintained high flow stress and improved energy absorption capacity compared to the conventional AMLS topologies such as OT and RD. Important findings from this work are listed as follows:

- Development of a high-fidelity yield surface to measure the value of the local stresses under global compressive loading in AMLS should account for both strut build direction and the intrinsic size effects.
- STA heat-treatment improved the yield strength for both OT and RD topologies by 42% and 56%, respectively. However, a 50% and 17% drop in flow stress was observed, beginning around 10% strain for both OT and RD topologies, respectively. Generally, the drop in flow stress is attributed to the damage localization in the struts with higher NET and higher tension-based elongation.
- There is a synergistic relationship between microstructure and topology. In other words, to gain complete control of the mechanical performance, it is necessary to move down in length-scale and understand the role of the constituent struts' microstructure in

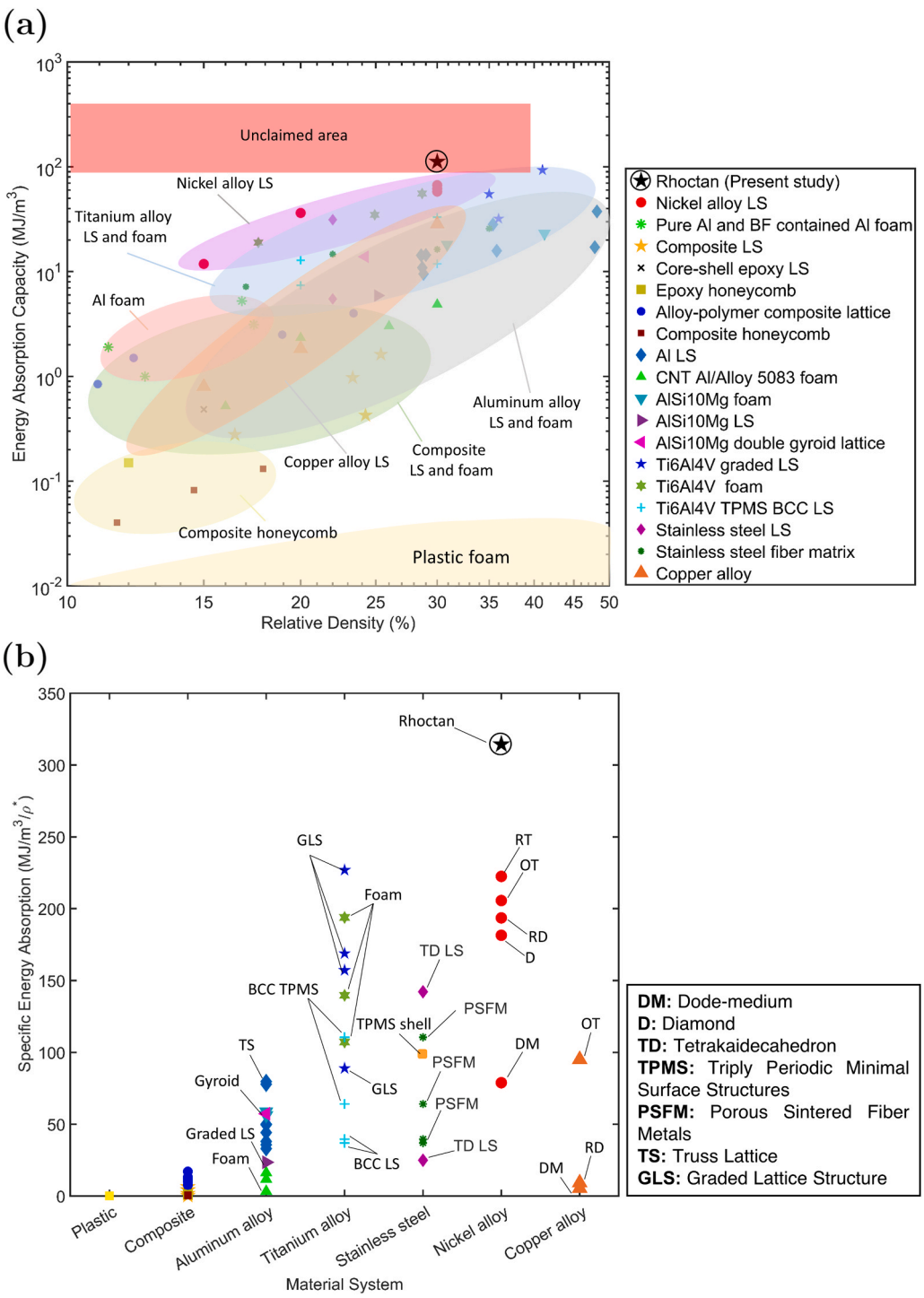

Fig. 17. Superior energy absorption capacity and high specific energy absorption properties of RTN topology. (a) Ashby plot style for energy absorption per unit volume versus relative density, (b) specific energy absorption properties of different material structures. Both charts compare the energy absorption of the new optimized topology against other most advanced metallic and composite foam and LS so far [56–71].

conjunction with the AMLS topology on the mechanical properties. Therefore, topology-microstructure-based optimization leads to improved structural integrity in AMLS.

- From a manufacturing perspective, in AMLS, diagonal struts are stronger than the vertical struts; from a deformation mechanism perspective, horizontal struts tend to undergo under tensile states of stress. Furthermore, due to strength differential effects in IN718, yield strength in tension is lower than yield strength in compression. Accordingly, damage more likely initiates from horizontal struts.
- The results reveal that NET is a deciding factor in the deformation and failure mechanisms of AMLS. It means the higher the value of NET during AMLS deformation, the more likely damage, and fracture in the form of the structural shear bands occurs. The is due to the low elongation of STA IN718 under tensile states of stress. By realizing this, the new topologies (RT and RTN) are designed in a way to reduce the NET and increase NEC. As a result, the newly designed topologies show ever-hardening behavior with no drop in the flow

stress, rather than commonly seen hardening followed by softening behavior in AMLS and metallic foams.

- In this study, NET+NEC, which represents the total number of elements involved in deformation, is used as a design variable. A lower value of NET+NEC during deformation means plastic strain and damage localization occurs in either struts or nodes. Hence, the design goal is to increase the value of NET+NEC throughout the entire deformation process to better distribute the applied load between all struts and nodes.
- STA IN718 has low ductility (less than 12% elongation under tensile loading); therefore, the lower the elongation in struts and nodes, the lower the likelihood of fracture leading to a drop in the stress-strain behavior. One effective way to hinder the elongation of struts and nodes beyond 10% is by imposing boundary conditions such as adding a bracing system to support the nodes and struts.
- Based on the deformation and failure mechanisms of OT and RD topologies with STA microstructure, two new topologies were introduced; RT and RTN. In both RT and RTN, (i) the number of horizontal struts was minimized, (ii) boundary conditions were imposed to support nodes and struts and act as an obstacle to passing the critical elongation for fracture.
- The deformation and failure behavior of RTN topology illustrates 53%, 25%, and 15% higher energy absorption capacity than OT, RD, and RT topologies, respectively. Moreover, no softening behavior was seen in the stress-strain behavior of the RTN topology. That indicates minor localized damage occurred in RTN under quasi-static compression loading. As a result, RTN topology is the most compatible topology with the STA microstructure.
- RTN samples exhibit a significantly higher energy absorption capacity per unit volume and unit mass, respectively, compared to other metallic and composite structures used in several previous studies. Therefore, the RTN topology has tremendous potential in high value-added industries such as aerospace and military that need high energy absorption capacity and structural integrity under compressive loading.

Declaration of Competing Interest

The authors declare that they have no known competing financial interests or personal relationships that could have appeared to influence the work reported in this paper.

Acknowledgment

This investigation was supported by Mechanics of Materials and Structures (MOMS) program at the National Science Foundation (NSF) under the Award Number: 1943465.

References

[1] M.P. Bendsoe, O. Sigmund, Topology Optimization: Theory, Methods, and Applications, Springer Science & Business Media, 2013.
[2] O. Sigmund, Topology optimization: a tool for the tailoring of structures and materials, Philos. Trans. R. Soc. Lond. Ser. A: Math., Phys. Eng. Sci. 358 (1765) (2000) 211–227.
[3] J.C. Maxwell, Xlv. on reciprocal figures and diagrams of forces. The London, Edinburgh, and Dublin, Philos. Mag. J. Sci. 27 (182) (1864) 250–261.
[4] L.J. Gibson, M.F. Ashby, Cellular Solids: Structure and Properties, Cambridge University Press, 1999.
[5] S.J. Li, Q.S. Xu, Z. Wang, W.T. Hou, Y.L. Hao, R. Yang, L.E. Murr, Influence of cell shape on mechanical properties of ti-6al-4v meshes fabricated by electron beam melting method, Acta Biomater. 10 (10) (2014) 4537–4547.
[6] S. Hyun, A.M. Karlsson, S. Torquato, A.G. Evans, Simulated properties of kagome and tetragonal truss core panels, Int. J. Solids Struct. 40 (25) (2003) 6989–6998.
[7] M.A. Wettergreen, B.S. Bucklen, B. Starly, E. Yuksel, W. Sun, M.A.K. Liebschner, Creation of a unit block library of architectures for use in assembled scaffold engineering, Comput. -Aided Des. 37 (11) (2005) 1141–1149.
[8] C. Yong, 3d texture mapping for rapid manufacturing, Comput. -Aided Des. Appl. 4 (6) (2007) 761–771.
[9] G. Savio, R. Meneghello, G. Concheri, Optimization of lattice structures for additive manufacturing technologies. In Advances on Mechanics, Design Engineering and Manufacturing, Springer, 2017, pp. 213–222.
[10] Z. Liu, M.A. Meyers, Z. Zhang, R.O. Ritchie, Functional gradients and heterogeneities in biological materials: design principles, functions, and bioinspired applications, Prog. Mater. Sci. 88 (2017) 467–498.
[11] D.J. Brackett, I.A. Ashcroft, R.D. Wildman, R.J.M. Hague, An error diffusion based method to generate functionally graded cellular structures, Comput. Struct. 138 (2014) 102–111.
[12] G. Wang, L. Shen, J. Zhao, H. Liang, D. Xie, Z. Tian, C. Wang, Design and compressive behavior of controllable irregular porous scaffolds: based on voronoi-tessellation and for additive manufacturing, ACS Biomater. Sci. Eng. 4 (2) (2018) 719–727.
[13] Y. Du, H. Liang, D. Xie, N. Mao, J. Zhao, Z. Tian, C. Wang, L. Shen, Design and statistical analysis of irregular porous scaffolds for orthopedic reconstruction based on voronoi tessellation and fabricated via selective laser melting (slm), Mater. Chem. Phys. 239 (2020), 121968.
[14] M. Fantini, M. Curto, F. De Crescenzio, A method to design biomimetic scaffolds for bone tissue engineering based on voronoi lattices, Virtual Phys. Prototyp. 11 (2) (2016) 77–90.
[15] H.-Y. Lei, J.-R. Li, Z.-J. Xu, Q.-H. Wang, Parametric design of voronoi-based lattice porous structures, Mater. Des. (2020), 108607.
[16] S.M. Giannitelli, D. Accoto, M. Trombetta, A. Rainer, Current trends in the design of scaffolds for computer-aided tissue engineering, Acta Biomater. 10 (2) (2014) 580–594.
[17] J. Sienkiewicz, P. Płatek, F. Jiang, X. Sun, A. Rusinek, Investigations on the mechanical response of gradient lattice structures manufactured via slm, Metals 10 (2) (2020).
[18] M.F. Ashby, T. Evans, N.A. Fleck, J.W. Hutchinson, H.N.G. Wadley, L.J. Gibson, Metal Foams: A Design Guide, Elsevier, 2000.
[19] L. Cheng, J. Liu, X. Liang, A.C. To, Coupling lattice structure topology optimization with design-dependent feature evolution for additive manufactured heat conduction design, Comput. Methods Appl. Mech. Eng. 332 (2018) 408–439.
[20] O. Sigmund, Materials with prescribed constitutive parameters: an inverse homogenization problem, Int. J. Solids Struct. 31 (17) (1994) 2313–2329.
[21] J.V. Carstensen, Topology Optimization Algorithms for Improved Manufacturability and Cellular Material Design.PhD thesis, Johns Hopkins University, 2017.
[22] A. Panesar, M. Abdi, D. Hickman, I. Ashcroft, Strategies for functionally graded lattice structures derived using topology optimisation for additive manufacturing, Addit. Manuf. 19 (2018) 81–94.
[23] R.M. Latture, R.X. Rodriguez, L.R. Holmes Jr., F.W. Zok, Effects of nodal fillets and external boundaries on compressive response of an octet truss, Acta Mater. 149 (2018) 78–87.
[24] B. Sarac, J. Ketkaew, D.O. Popnoe, J. Schroers, Honeycomb structures of bulk metallic glasses, Adv. Funct. Mater. 22 (15) (2012) 3161–3169.
[25] Y. Tang, Y.F. Zhao, Lattice-skin structures design with orientation optimization, Proc. Solid Free. Fabr. Symp. (2015) 1378–1393.
[26] J. Wu, W. Wang, and X. Gao, Design and optimization of conforming lattice structures. arXiv:1905.02902, 2019.
[27] Z. Wu, L. Xia, S. Wang, T. Shi, Topology optimization of hierarchical lattice structures with substructuring, Comput. Methods Appl. Mech. Eng. 345 (2019) 602–617.
[28] R.-q. Feng, F.-c. Liu, W.-j. Xu, M. Ma, Y. Liu, Topology optimization method of lattice structures based on a genetic algorithm, Int. J. Steel Struct. 16 (3) (2016) 743–753.
[29] W. Chen, X. Zheng, S. Liu, Finite-element-mesh based method for modeling and optimization of lattice structures for additive manufacturing, Materials 11 (11) (2018) 2073.
[30] Y. Du, H. Li, Z. Luo, Q. Tian, Topological design optimization of lattice structures to maximize shear stiffness, Adv. Eng. Softw. 112 (2017) 211–221.
[31] C. Schumacher, B. Bickel, J. Rys, S. Marschner, C. Daraio, M. Gross, Microstructures to control elasticity in 3d printing, ACM Trans. Graph. (TOG) 34 (4) (2015) 1–13.
[32] Y. Wang, H. Xu, D. Pasini, Multiscale isogeometric topology optimization for lattice materials, Comput. Methods Appl. Mech. Eng. 316 (2017) 568–585.
[33] R. Sivapuram, P.D. Dunning, H.A. Kim, Simultaneous material and structural optimization by multiscale topology optimization, Struct. Multidiscip. Optim. 54 (5) (2016) 1267–1281.
[34] D. Wang, M.M. Abdalla, Z.-P. Wang, Z. Su, Streamline stiffener path optimization (sspo) for embedded stiffener layout design of non-uniform curved grid-stiffened composite (ncgc) structures, Comput. Methods Appl. Mech. Eng. 344 (2019) 1021–1050.
[35] Q. Xia, T. Shi, A cascadic multilevel optimization algorithm for the design of composite structures with curvilinear fiber based on shepard interpolation, Compos. Struct. 188 (2018) 209–219.
[36] J. Wu, A. Clausen, O. Sigmund, Minimum compliance topology optimization of shell-infill composites for additive manufacturing, Comput. Methods Appl. Mech. Eng. 326 (2017) 358–375.
[37] J. Wu, N. Aage, R. Westermann, O. Sigmund, Infill optimization for additive manufacturing?approaching bone-like porous structures, IEEE Trans. Vis. Comput. Graph. 24 (2) (2017) 1127–1140.
[38] K. Hazeli, B. Babamiri, J. Indeck, A. Minor, H. Askari, Microstructure-topology relationship effects on the quasi-static and dynamic behavior of additively manufactured lattice structures, Mater. Des. 176 (2019), 107826.

[39] ASTM International. F3055–14a standard specification for additive manufacturing nickel alloy (uns n07718) with powder bed fusion. West Conshohocken, PA; ASTM International, 2014. https://doi.org/10.1520/F3055–14A.
[40] B.B. Babamiri, H. Askari, K. Hazeli, Deformation mechanisms and post-yielding behavior of additively manufactured lattice structures, Mater. Des. 188 (2020), 108443.
[41] V.S. Deshpande, N.A. Fleck, Isotropic constitutive models for metallic foams, J. Mech. Phys. Solids 48 (6–7) (2000) 1253–1283.
[42] V.D. Fachinotti, A.A. Anca, A. Cardona, A method for the solution of certain problems in least squares, Int J. Numer. Method Biomed. Eng. 27 (4) (2011) 595–607.
[43] D.W. Marquardt, An algorithm for least-squares estimation of nonlinear parameters, J. Soc. Ind. Appl. Math. 11 (2) (1963) 431–441.
[44] J. Dzugan, M. Seifi, R. Prochazka, M. Rund, P. Podany, P. Konopik, J. J. Lewandowski, Effects of thickness and orientation on the small scale fracture behaviour of additively manufactured ti-6al-4v, Mater. Charact. 143 (2018) 94–109.
[45] A. Roach, B. White, A. Garland, B. Jared, J. Carroll, B. Boyce, Size-dependent stochastic tensile properties in additively manufactured 316l stainless steel, Addit. Manuf. (2020).
[46] G. Demeneghi, B. Barnes, P. Gradl, J.R. Mayeur, K. Hazeli, Size effects on microstructure and mechanical properties of additively manufactured copper-chromium-niobium (grcop-42) alloy, Mater. Sci. Eng. A (2021).
[47] J. Gockel, L. Sheridan, B. Koerper, B. Whip, The influence of additive manufacturing processing parameters on surface roughness and fatigue life, Int. J. Fatigue 124 (2019) 380–388.
[48] J. Slotwinski, E. Garboczi, K. Hebenstreit, Porosity measurements and analysis for metal additive manufacturing process control, J. Res. Natl. Inst. Stand. Technol. 119 (2014) 494–528.
[49] R. Shrestha, N. Shamsaei, M. Seifi, N. Phan, An investigation into specimen property to part performance relationships for laser beam powder bed fusion additive manufacturing, Addit. Manuf. 29 (2019), 100807.
[50] V.S. Deshpande, M.F. Ashby, N.A. Fleck, Foam topology: bending versus stretching dominated architectures, Acta Mater. 49 (6) (2001) 1035–1040.
[51] F.E.A. Abaqus, Abaqus inc.Providence, Rhode Island, United States, 2017.
[52] G.R. Johnson, W.H. Cook, Fracture characteristics of three metals subjected to various strains, strain rates, temperatures and pressures, Eng. Fract. Mech. 21 (1) (1985) 31–48.
[53] Ar. Hillerborg, M. Modeer, P.-E. Petersson, Analysis of crack formation and crack growth in concrete by means of fracture mechanics and finite elements, Cem. Concr. Res. 6 (6) (1976) 773–781.
[54] B.B. Babamiri, J. Indeck, G. Demeneghi, J. Cuadra, K. Hazeli, Quantification of porosity and microstructure and their effect on quasi-static and dynamic behavior of additively manufactured inconel 718, Addit. Manuf. (2020), 101380.
[55] S.Y. Liu, H.Q. Li, C.X. Qin, R. Zong, X.Y. Fang, The effect of energy density on texture and mechanical anisotropy in selective laser melted inconel 718, Mater. Des. (2020), 108642.
[56] D. Yang, Z. Zhang, X. Chen, X. Han, T. Xu, X. Li, J. Ding, H. Liu, X. Xia, Y. Gao, et al., Quasi-static compression deformation and energy absorption characteristics of basalt fiber-containing closed-cell aluminum foam, Metals 10 (7) (2020) 921.
[57] S. Yuan, C.K. Chua, K. Zhou, 3d-printed mechanical metamaterials with high energy absorption, Adv. Mater. Technol. 4 (3) (2019), 1800419.
[58] J. Mueller, J.R. Raney, K. Shea, J.A. Lewis, Architected lattices with high stiffness and toughness via multicore-shell 3d printing, Adv. Mater. 30 (12) (2018), 1705001.
[59] B.G. Compton, J.A. Lewis, 3d-printing of lightweight cellular composites, Adv. Mater. 26 (34) (2014) 5930–5935.
[60] X. Zhang, J. Yao, B. Liu, J. Yan, L. Lu, Y. Li, H. Gao, X. Li, Three-dimensional high-entropy alloy-polymer composite nanolattices that overcome the strength-recoverability trade-off, Nano Lett. 18 (7) (2018) 4247–4256.
[61] H. Wang, Y. Fu, M. Su, H. Hao, Effect of structure design on compressive properties and energy absorption behavior of ordered porous aluminum prepared by rapid casting, Mater. Des. 167 (2019), 107631.
[62] A. Aldoshan, S. Khanna, Effect of relative density on the dynamic compressive behavior of carbon nanotube reinforced aluminum foam, Mater. Sci. Eng.: A 689 (2017) 17–24.
[63] L. Stanev, B. Drenchev, A. Yotov, R. Lazarova, Compressive properties and energy absorption behaviour of alsi10mg open-cell foam, J. Mater. Sci. Technol. 22 (1) (2014) 44–53.
[64] I. Maskery, N.T. Aboulkhair, A.O. Aremu, C.J. Tuck, I.A. Ashcroft, R.D. Wildman, R.J.M. Hague, A mechanical property evaluation of graded density al-si10-mg lattice structures manufactured by selective laser melting, Mater. Sci. Eng.: A 670 (2016) 264–274.
[65] I. Maskery, N.T. Aboulkhair, A.O. Aremu, C.J. Tuck, I.A. Ashcroft, Compressive failure modes and energy absorption in additively manufactured double gyroid lattices, Addit. Manuf. 16 (2017) 24–29.
[66] S.Y. Choy, C.-N. Sun, K.F. Leong, J. Wei, Compressive properties of functionally graded lattice structures manufactured by selective laser melting, Mater. Des. 131 (2017) 112–120.
[67] B. Xie, Y.Z. Fan, T.Z. Mu, B. Deng, Fabrication and energy absorption properties of titanium foam with cacl2 as a space holder, Mater. Sci. Eng.: A 708 (2017) 419–423.
[68] C. Bonatti, D. Mohr, Mechanical performance of additively-manufactured anisotropic and isotropic smooth shell-lattice materials: simulations & experiments, J. Mech. Phys. Solids 122 (2019) 1–26.
[69] M. Zhao, F. Liu, G. Fu, D.Z. Zhang, T. Zhang, H. Zhou, Improved mechanical properties and energy absorption of bcc lattice structures with triply periodic minimal surfaces fabricated by slm, Materials 11 (12) (2018) 2411.
[70] T. Zhong, K. He, H. Li, L. Yang, Mechanical properties of lightweight 316l stainless steel lattice structures fabricated by selective laser melting, Mater. Des. 181 (2019), 108076.
[71] J.C. Qiao, Z.P. Xi, J.Y. Wang, J.L. Zhu, Compressive property and energy absorption of porous sintered fiber metals, Mater. Trans. 49 (12) (2008) 2919–2921.